

Calibration of ILIDS and PDPA droplet sizing
systems and their application to the breakup of
impacting water and air jets

Sebastian Kosch, University of Toronto

2015

List of symbols and abbreviations

| | |
|-----------------------|---|
| $\Delta\vartheta$ | Angular spacing between two adjacent fringes |
| Δz | Distance along the z -axis between the focal plane of the lens and the light sheet |
| \hat{N}_{fr} | Peak fringe count measured |
| χ | Scalar value relating the fringe count N_{fr} to the physical diameter of the particle D_d |
| D_i | Diameter (in pixels) of the defocussed image |
| D_{padded} | Width (in pixels) of the padded input to the Fourier transform |
| D_d | Physical diameter of the particle (here: droplet) |
| $d_{p,x}; d_{p,y}$ | Physical dimensions of a pixel on the camera's CCD sensor |
| f_{peak} | Peak frequency |
| M | Magnification |
| N_{fr} | Number of fringes |
| s_x | Distance, in pixels, between two adjacent fringes |

Introduction

1.1 Why spray sizing is important

Fluid sprays find application in numerous designs, ranging from fuel injection and coating systems to medical and printing devices. Often, the droplet size is a major factor in how well these systems perform. Consequently, measuring the characteristics of a given spray to a useful degree of accuracy is an important task with relevance to several areas of mechanical engineering.

Due to the behaviour and size of the droplets in typical sprays, only non-intrusive instrumentation methods come into question. The most popular techniques rely on illumination of the spray with laser light. The droplets scatter the light, and it is picked up by a set of detectors, such as photomultiplier tubes or digital cameras. Depending on the position of the detectors, the motion of the droplets, their size, and the laser light's known properties, the detected patterns can be processed to yield information about the spray's characteristics.

While countless different optical setups are in use in laboratories the world over, all of them rely on the same fundamental optical principles governing the scattering of light. This paper aims to offer a high-level derivation of these principles.

1.2 What our contributions in this paper are

- Our contributions:
 - Pupillary magnification has to be taken into account
 - Circle detection algorithm is crap

1.3 What other work has been done in this area

Experimental setup

- What kinds of setups there are
 - Our setup:

2.1 Dantec system

- Dantec system

2.2 PDPA system

- TSI system

Mie scattering

In this chapter, we will discuss some of the fundamentals of Mie scattering. The majority of the equations and derivations herein are adapted directly from [?]. For the purposes of this discussion, we will model light as a coupled pair of electrical and magnetic fields, \mathbf{E} and \mathbf{B} , which at every point in space obey Maxwell's equations

$$\nabla \cdot \mathbf{E} = \frac{\rho}{\epsilon_0} \quad (3.1)$$

$$\nabla \cdot \mathbf{B} = 0 \quad (3.2)$$

$$\nabla \times \mathbf{E} = -\frac{\partial \mathbf{B}}{\partial t} \quad (3.3)$$

$$\nabla \times \mathbf{B} = \mu_0 \sigma \mathbf{E} + \mu_0 \epsilon_0 \frac{\partial \mathbf{E}}{\partial t}, \quad (3.4)$$

where the constants ϵ_0 and μ_0 represent the electric permittivity and magnetic permeability in vacuum, respectively; ρ is the local charge density, and σ is the electric conductivity (such that $\sigma \mathbf{E} = \mathbf{J}$ is the current density).

Electromagnetic radiation propagates in a direction \mathbf{S} orthogonal to the planes of oscillation of \mathbf{E} and \mathbf{B} , which are themselves orthogonal to one another:

$$\mathbf{S} = \mathbf{E} \times \mathbf{B}. \quad (3.5)$$

\mathbf{S} is called the *Poynting vector*.

Note that this definition leaves \mathbf{S} invariant to a rotation of \mathbf{E} and \mathbf{B} around \mathbf{S} . The rotation angle is called *polarization* and need not be constant along the line of propagation ("circular polarization"), although we will here assume that it is ("linear polarization") to simplify our derivations. This assumption is justified in typical spray characterization ap-

plications, for gas lasers use *Brewster windows* both as mirrors and output windows which act as polarization filters.

We will also assume here that \mathbf{S} is approximately constant over the surface of the droplet. In other words, we assume the incoming light wave to be plane. Whether this is a reasonable assumption depends on the configuration of the laser optics, on the width of the laser beams and on the size of the droplet. We will see in Section ?? that more complex models without this assumption can be used, but they are not suitable for showcasing the fundamental concepts behind droplet light scattering. Finally, we assume the droplet in question to be perfectly spherical.

3.0.1 Scattering phenomena

When light hits a spherical, transparent droplet, three phenomena can be observed:

1. Diffraction
2. Reflection
3. Refraction

We will consider each one in this paper, and derive its influence on the scattered field.

In the following discussion, we will use a coordinate system centered on the droplet. Let the z -axis be aligned with the direction of the plane wave incident on the droplet, and define the rotation of the x - y -plane to be at an arbitrary but fixed angle with respect to light source and detector. Consider then an infinitesimally small light ray scattered by the droplet. We shall designate the direction of the scattered ray to be at a deviation angle φ with respect to the x -axis, and to be at a deviation angle θ with respect to the z -axis.

We also define the plane between the scattered direction and the scattered direction's projection onto the x - y -plane as the *scattering plane*. This allows us to treat any incident polarization as a linear combination of polarization parallel to that scattering plane (θ -field) and perpendicular to it (φ -field).

3.1 Diffraction

Diffraction, sometimes described as the “bending” of light waves, is the phenomenon observed when plane waves – even material waves – encounter the edge of an obstacle and

spread out spherically behind it. While most of the scattered intensity is focussed along the original wave path, the scattered fields from two or more edges will interfere behind the obstacle and create an intensity pattern dependent on both the wavelength and the edges' separation.

A droplet in a plane wave, just like a hole of the same size, has one circular edge (or a set of infinitely many point-sized edges arranged in a circle). The diffracted fields interfere behind the particle, as shown in Figure ??, to form a periodic intensity pattern.

The viability of exploiting diffraction as a spray characterization principle is limited, because the phenomenon is strongest when droplet sizes are close to the light's wavelength. We will thus focus here on scattering phenomena relevant to techniques such as *Phase Doppler Anemometry* and *Interferometric Particle Imaging*.

3.2 Reflection and refraction

Detectors used in spray diagnostics are ultimately based on the photoelectric effect, and thus sensitive only to incident light intensity. This is the case both for CMOS or CCD cameras used in interferometric techniques and for photovoltaic cascade amplifiers commonly used in Phase Doppler setups. As a result, we are interested in accurately modelling the light intensity at a location $\langle\varphi, \theta, z\rangle$.

A general description of the scattering process would trace a ray of light through the droplet. At every encounter with an interface (air→water, or water→air inside the droplet), some of the light is *reflected off* the interface and some is *refracted through* the interface. When first incident, the refracted light ray is cast *into* the droplet; subsequent scattering events will refract some light *out* of the droplet while the remainder continues scattering within the droplet until all energy is refracted out or absorbed as heat. Scattering events are enumerated; the *scattering order N* refers to the N^{th} reflection/refraction.

Total intensity at any location is a function both of the intensity of all infinitesimal light rays scattered onto that location, but also of the phases of those light rays, as two equally intense light rays will extinguish one another if they are in opposite phases. We will thus derive expressions for both intensity and phase of infinitesimal light rays scattered through the droplet.

3.2.1 Intensity from interface separation

Consider an infinitesimal ray incident, at an angle ϑ_i , on the surface of the droplet. We are interested in the respective proportions of light reflected and refracted.

Following the continuity requirement for components of \mathbf{E} and \mathbf{B} parallel and perpendicular to the droplet's interface (depending on the polarization component), and the conservation of energy, we can arrive at *Fresnel equations*:

$$r_\theta = \frac{m \cos \vartheta_i - \cos \vartheta_t}{m \cos \vartheta_i + \cos \vartheta_t}, \quad r_\varphi = \frac{\cos \vartheta_i - m \cos \vartheta_t}{\cos \vartheta_i + m \cos \vartheta_t} \quad (3.6)$$

with $\vartheta_t = \arcsin\left(\frac{\sin \vartheta_i}{m}\right)$, and m the relative refractive index of droplet and medium (e.g. $m = 1.33/1.0$ for the water→air transition).

Squaring these numbers yields a reflectance coefficient $R = |r|^2$ for both polarization directions, and since $R + T = 1$, the computation of T is then trivial.

3.2.2 Intensity from geometry

An infinitesimal plane wave ray incident on a curved surface will inevitably experience deviation into a diverging ray (convex surface) or a converging ray (concave surface).

Consider Figure 3.1. An annular ray of surface area dA_i is incident on the droplet of radius r_p . The first-order scattering is shown: the infinitesimal thickness of the ray results in an annular illuminated surface region between the angles ϑ_i and $\vartheta_i + d\vartheta_i$ of area

$$dA_i = \pi r_p^2 \sin(2\vartheta_i + d\vartheta_i) \sin(d\vartheta_i) \quad (3.7)$$

The reflected portion of the light diverges; its cross-section has a divergence angle of $2 d\vartheta_i$.

We can now imagine a sphere around the droplet. Its radius equals the distance to the detector, r_{pr} . The area of that sphere illuminated by the reflected portion of dA_i can be geometrically shown to be

$$dA^{(1)} = 4\pi r_{pr}^2 \sin(2\vartheta_i + d\vartheta_i) \sin(d\vartheta_i). \quad (3.8)$$

The ratio between them is then

$$I_r^{(1)} = \frac{dA_i}{dA^{(1)}} = I_w \frac{r_p^2}{4r_{pr}^2}. \quad (3.9)$$

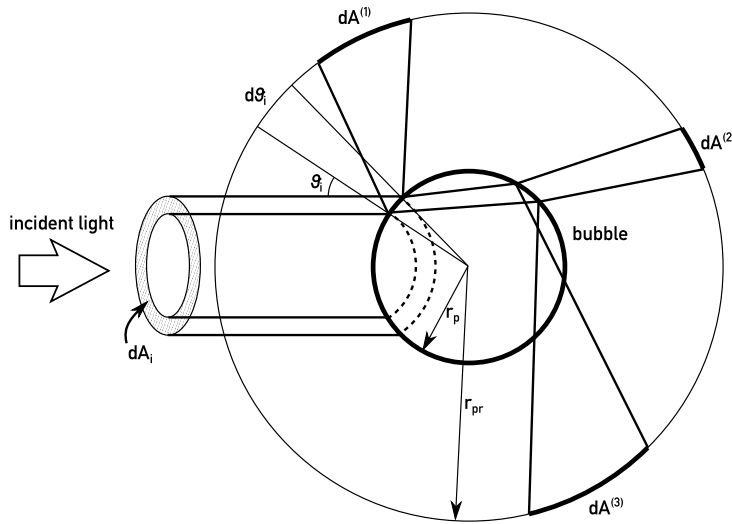


Figure 3.1: Ray divergence due to curved interfaces. Note that here a bubble in water is used instead of a droplet. Adapted from []

The ratio r_p^2/r_{pr}^2 varies based on the setup; to normalize it we place a point source of the same intensity of light at the centre of the droplet and consider its intensity at r_p^2 :

$$I_P = I_w \frac{r_p^2}{r_{pr}^2} \quad (3.10)$$

We drop this term from equation (3.9) and arrive at a fixed fraction, or *gain factor*, of $G^{(1)} = \frac{1}{4}$. This number represents the “dilution of energy” associated with the divergence inherent in reflection off a curved surface.

Similar gain factors can be derived for any other scattering order N of light leaving the droplet:

$$G^{(N)} = \left| \frac{\sin \vartheta_i \cos \vartheta_i}{\sin D^{(N)}} \left(2 \frac{(N-1) \cos \vartheta_i}{m \cos \vartheta_t} - 2 \right)^{-1} \right| \quad (3.11)$$

with

$$D^{(N)} = 2(N-1) \arcsin \left(\frac{\sin \vartheta_i}{m} \right) - (N-2)\pi - 2\vartheta_i. \quad (3.12)$$

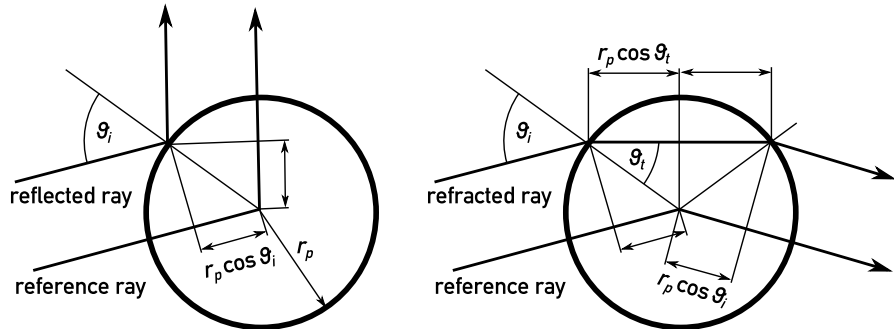


Figure 3.2: Path length differences, adapted from ?]

3.2.3 Path-length differences

Whether light rays interfere constructively or destructively depends on the phase difference between them. Since all rays are generated in phase in the laser cavity, possible phase differences must be due to path length differences, distortion of the wave (focal shift) or reflection effects. We shall first discuss the treatment of path lengths.

To effectively compare path lengths between various rays, it is practical to establish a reference path length for common comparison. This reference ray is typically pictured as passing through the center of the droplet – an optical anomaly as it were, but geometrically useful.

A ray incident at an angle ϑ_i and reflected off the surface of the particle then has a path length $2kr_p \cos \vartheta_i$ shorter than that of the reference ray, where k is the wave number of the light ray. This situation is illustrated in Figure 3.2a.

A more general equation for phase length difference is

$$\phi^{(N)} = 2kr_p(\cos \vartheta_i - (N - 1)m \cos \vartheta_i), \quad (3.13)$$

where ϕ stands for the phase difference and is not to be confused with the scattering plane's orientation φ .

3.2.4 Phase shifts at reflection

A ray's phase is further affected upon reflection. This relationship is quite complex and depends on the critical and Brewster angles between the two media, the polarization angle

and the relative refractive index. For example, the phase is flipped when a ray is reflected off a medium with higher refractive index (such as a water droplet), if the ray is polarized parallel to the interface and the incident angle does not exceed the Brewster angle. Similar relationships hold for all other conditions.

The derivations of these phase change formulae follow from the Fresnel equations (3.6) shown above and from the understanding that incident and refracted amplitudes must always sum to the refracted amplitude (which is zero for total reflection), i.e. continuity of amplitudes across interfaces. They are widely published (e.g. [?]) and algebraically straightforward but lengthy, and thus not included here.

3.2.5 Phase shifts through focussing

While the phase of a plane wave ray does not change (except for the wave's propagation through time and space), the phase of a diverging or converging ray is affected by the angle determining the ray width change as follows:

$$\phi^{(N)} = \pi \left((N - 1) - \frac{1}{2} \left[1 + \operatorname{sgn} \left(\frac{\partial D^{(N)}}{\partial \vartheta} \right) \right] \right), \quad (3.14)$$

The derivation given in [?] explains this as a phase shift of $\pi/2$ whenever an astigmatic ray passes a focal line.

3.2.6 Scattering functions

The expressions given in the above sections can be combined into *scattering functions* for both polarization directions as follows:

$$S_1^{(N)} = \sqrt{i_\varphi^{(N)}} \exp(j\phi_\varphi^{(N)}), \quad S_2 = \sqrt{i_\theta^{(N)}} \exp(j\phi_\theta^{(N)}). \quad (3.15)$$

Here, i is the intensity coefficient

$$i_{\theta,\varphi}^{(N)}(\lambda, d_p, m, \vartheta_i) = \left(\frac{\pi d_p}{\lambda} \right)^2 \alpha_{\theta,\varphi}^{(N)} G^{(N)} \quad (3.16)$$

defined in terms of wavelength λ , droplet diameter d_p , gain factor $G^{(N)}$ as given in (3.11) above, and $\alpha^{(N)}$, which is a shorthand for the product of all applicable reflectance and trans-

mittance coefficients:

$$\alpha_{\theta,\varphi}^{(N)} = \begin{cases} R_{\theta,\varphi}, & N = 1 \\ R_{\theta,\varphi}^{N-2} T_{\theta,\varphi}^2, & N \geq 2 \end{cases}. \quad (3.17)$$

The $\exp(j\phi_{\varphi,\theta}^{(N)})$ terms represent the phase shift added to the wave function term in (3.18)

We can use these two-component scattering functions to write a full expression relating the incident light wave \mathbf{E}_i in its components $\langle E_{ix}, E_{iy} \rangle$ to the wave received by the detector, \mathbf{E}_r :

$$\mathbf{E}_r = \frac{\exp(-jkr_{pr})}{kr_{pr}} \begin{bmatrix} \cos \beta_{\theta x} & \cos \beta_{\varphi x} \\ \cos \beta_{\theta y} & \cos \beta_{\varphi y} \end{bmatrix} \quad (3.18)$$

$$\begin{bmatrix} \sum_{N=0}^{\infty} S_1^{(N)} & 0 \\ 0 & \sum_{N=0}^{\infty} S_2^{(N)} \end{bmatrix} \times \begin{bmatrix} -\sin \varphi & \cos \varphi \\ \cos \varphi & \sin \varphi \end{bmatrix} \begin{bmatrix} E_{ix} \\ E_{iy} \end{bmatrix} \quad (3.19)$$

The first term evaluates to a sinusoid function corresponding to the scalar component of the light wave. The second term (and first matrix) represents the geometrical relationship between the light source and the detector, expressed in terms of the off-angle β . Similarly, the matrix in φ represents the angle between light source and droplet. By multiplying the β matrix with the appropriate scattering functions (which are summed over all scattering orders N), we arrive at the correct intensity at the detector's location.

3.3 Mie theory

The above derivations, commonly termed *geometrical optics*, are physically intuitive and therefore useful in the understanding and design of measurement instrumentation. Geometrical optics, however, are limited to incident waves that are both plane and much smaller in wavelength than the droplet diameter. A more general approach is therefore desirable for carrying out detailed numerical simulations.

Such a numerical system was developed independently by Ludvig Lorenz and Gustav Mie based on analytical solutions presented here briefly. The Mie scattering theory decomposes the incoming light into an infinite series of not plane, but spherical waves concentric with the droplet. The spherical waves are not uniform; their dependence depends on the angle ϑ .

The derivation in scalar terms assumes a scalar field magnitude ψ that solves

$$\nabla^2 \psi + k_m^2 \psi = 0 \quad (3.20)$$

where k_m^2 is the magnitude of the field in the surrounding medium.

In spherical coordinates, this leads to

$$\frac{1}{r^2} \frac{\partial}{\partial r} (r^2 \frac{\partial \psi}{\partial r}) + \frac{1}{r^2 \sin \vartheta} \frac{\partial}{\partial \vartheta} (\sin \vartheta \frac{\partial \psi}{\partial \vartheta}) + \frac{1}{r^2 \sin^2 \vartheta} \frac{\partial^2 \psi}{\partial \varphi^2} + k_m^2 \psi = 0 \quad (3.21)$$

Which is solved by

$$\psi(r, \vartheta, \varphi) = R(r)\Theta(\vartheta) \exp(\pm im\varphi) \quad (3.22)$$

according to ?].

Solving for the function governing angular dependence, $\Theta(\vartheta)$, leads to Legendre polynomials. Polar plots of the first five such functions of both types are shown in Figure 3.3.

Solving for $R(r)$, the function describing the intensity of the spherical waves as it drops with distance from the droplet, leads to vector spherical harmonics. Two-dimensional plots of a few orders of such “Riccati-Bessel functions” are shown in Figure 3.4.

Each partial wave, in turn, represents the sum of scattering effects up to some scattering order N (in practice, no infinite sum can be taken; the maximum scattering order to achieve negligible errors depends on the relative wavelength). With every refraction out of the droplet – thus adding to the total external field – the *internal* partial wave loses intensity according to respective reflectance and transmittance values.

The complete model, then, provides a semi-closed expression for the scattering func-

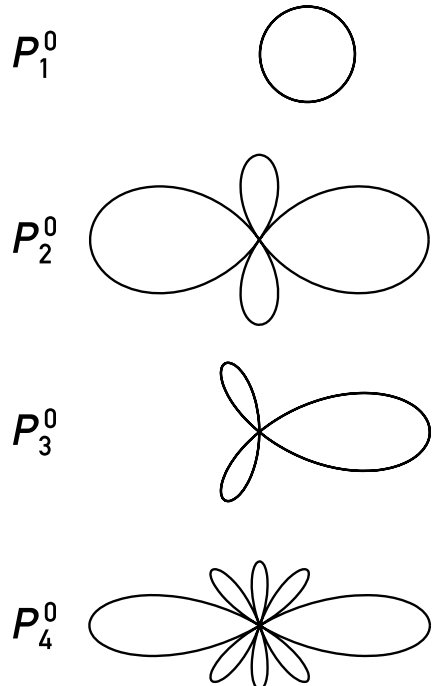


Figure 3.3: A few associated Legendre polynomials $\Theta(\vartheta)$ of order zero (here labelled P). Incident light is coming from the left.

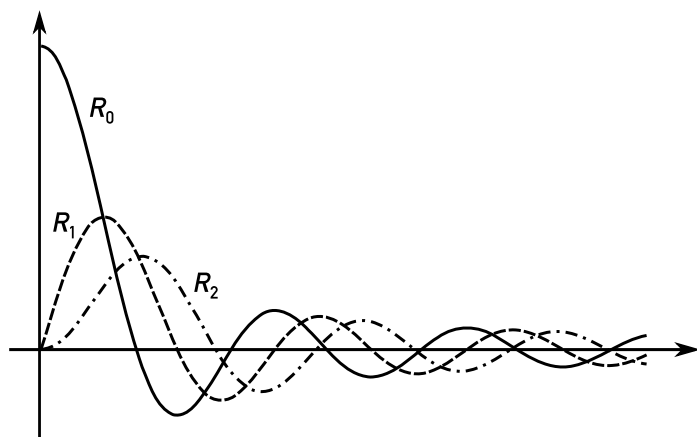


Figure 3.4: Some Riccati-Bessel functions governing the radial decay of the partial waves.

tions S_1 and S_2 :

$$S_1(\theta) = \sum_{n=1}^{\infty} a_n \pi_n(\theta) + b_n \tau_n(\theta) \quad (3.23)$$

$$S_2(\theta) = \sum_{n=1}^{\infty} a_n \tau_n(\theta) + b_n \pi_n(\theta) \quad (3.24)$$

$$a_n = \frac{2n+1}{2n(n+1)} (1 - R_{a_n}^{MM} - \sum_{p=2}^{\infty} T_{a_n}^{MP} (R_{a_n}^{PP})^{p-2} T_{a_n}^{PM}) \quad (3.25)$$

$$b_n = \frac{2n+1}{2n(n+1)} (1 - R_{b_n}^{MM} - \sum_{p=2}^{\infty} T_{b_n}^{MP} (R_{b_n}^{PP})^{p-2} T_{b_n}^{PM}) \quad (3.26)$$

$$\text{e.g. } R_{b_n}^{PP} = \frac{\zeta_n(m \frac{\pi d_p}{\lambda}) \zeta'_n(\frac{\pi d_p}{\lambda}) - m \zeta_n(\frac{\pi d_p}{\lambda}) \zeta'_n(m \frac{\pi d_p}{\lambda})}{-\frac{\pi d_p}{\lambda} \xi_n(m \frac{\pi d_p}{\lambda}) \zeta'(\frac{\pi d_p}{\lambda}) + m \zeta_n(\frac{\pi d_p}{\lambda}) \frac{\pi d_p}{\lambda} \xi'(m \frac{\pi d_p}{\lambda})} \quad (3.27)$$

where PP stands for interal reflection, MM external reflection, and MP and PM for refraction into and out of the particle, respectively. The expression for $R_{b_n}^{PP}$ is shown above to illustrate the coefficents' form. Note that in the above equations, π and τ are associated Legendre functions and ζ and ξ are Riccati-Bessel functions.

3.3.1 Results

Some numerical results are presented in Fig. 3.5 below.

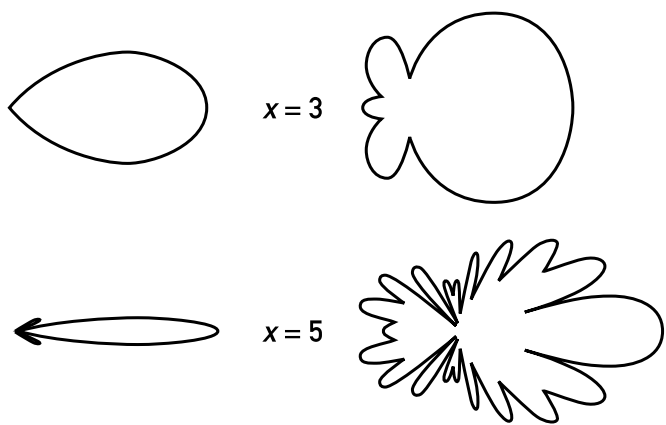


Figure 3.5: Scattered light intensity based on light incident from the left on a spherical particle of size parameters $x = 3$ and $x = 5$, where $x = \frac{\pi D_{dm}}{\lambda}$. Only perpendicularly polarized light intensities are shown. Right column shows logarithmically scaled intensities. Figure adapted from [?].

Monodisperse droplet generation

To calibrate any droplet sizing device, we need droplets of known and uniform size. Sprays or streams of such uniform droplets are called *monodisperse*, and many different varying approaches to generating them have been proposed, each one with advantages and drawbacks.

The most basic type of droplet generator is a capillary tube, for instance a hypodermic needle or a pulled glass pipette. Droplets are generated as the liquid flows through the tube due to its own weight. As the liquid leaves the tube, it wets the tip of the tube and forms a bead held together by surface tension. Eventually, the bead's gravitational forces overcome the attraction to the tube surface, and the drop separates from the tube.

Given a liquid and its physical properties, the only remaining controllable variable is the diameter of the capillary tube tip. As a rule, droplets generated in this fashion will be significantly larger than the tube diameter from which they grow. Most droplet generators are designed to prevent this from happening:

- *Aerodynamic* droplet generators use coaxial air flow to shear the forming droplet off of the capillary tip before it can grow to full size.
- *On-demand* droplet generators use a pressure pulse to eject a fixed amount of liquid out of the capillary (or other orifice).
- *Continuous-stream* droplet generators use mechanical vibrations to break up a continuous jet of liquid emanating from the capillary into monodisperse droplets.

More exotic types of droplet generators exist: ?] suggested that water falling on spinning

disks is propelled outwards, forming nearly monodisperse droplets, and several improved designs have been published since. Another approach, e.g. used by [?], involves mechanized dipping of a needle into a liquid reservoir, and then flicking it so as to produce one droplet.

4.1 Aerodynamic droplet generators

[?] provide a history of aerodynamic designs: the first design was published in 1947 by [?]; [?] later improved on it by using time-controlled air pulses instead of a continuous flow. Coggins and Baker [?] have proposed a more elaborate apparatus with variable air and liquid flow and adjustable needle position.

4.1.1 Stry design

Initial tests based on a design by [?] showed that the ability of the instrument to produce droplets below $600 \mu\text{m}$ depends entirely on the precision with which the flow of water and air can be controlled.

4.2 On-demand drop generators

Drop-on-demand technology finds its most important application in printing. Indeed, the most prominent designs representative of this category are the thermal droplet generators found in most household inkjet printers, invented by [?]. At least one research group, [?], has succeeded in repurposing an old inkjet print head for laboratory droplet generation.

Less widespread, but more flexible in a research setting, are on-demand generators driven by the contraction of piezoelectric elements, such as those proposed by [?] or [?]. Excellent reviews on drop-on-demand designs were published by Le and Lee [? ?].

A curious third type of on-demand generator by [?] uses a short pulse of pressurized air, controlled by a solenoid valve, to eject a small amount of liquid through an orifice.

While drop-on-demand generators are a crucial component in applications like inkjet printing or microfluidics, they tend to suffer from aspirated air bubbles, pileup of liquid around the nozzle tip, clogging, and other issues thwarting reliable drop expulsion unless manufactured and operated with great attention to detail.

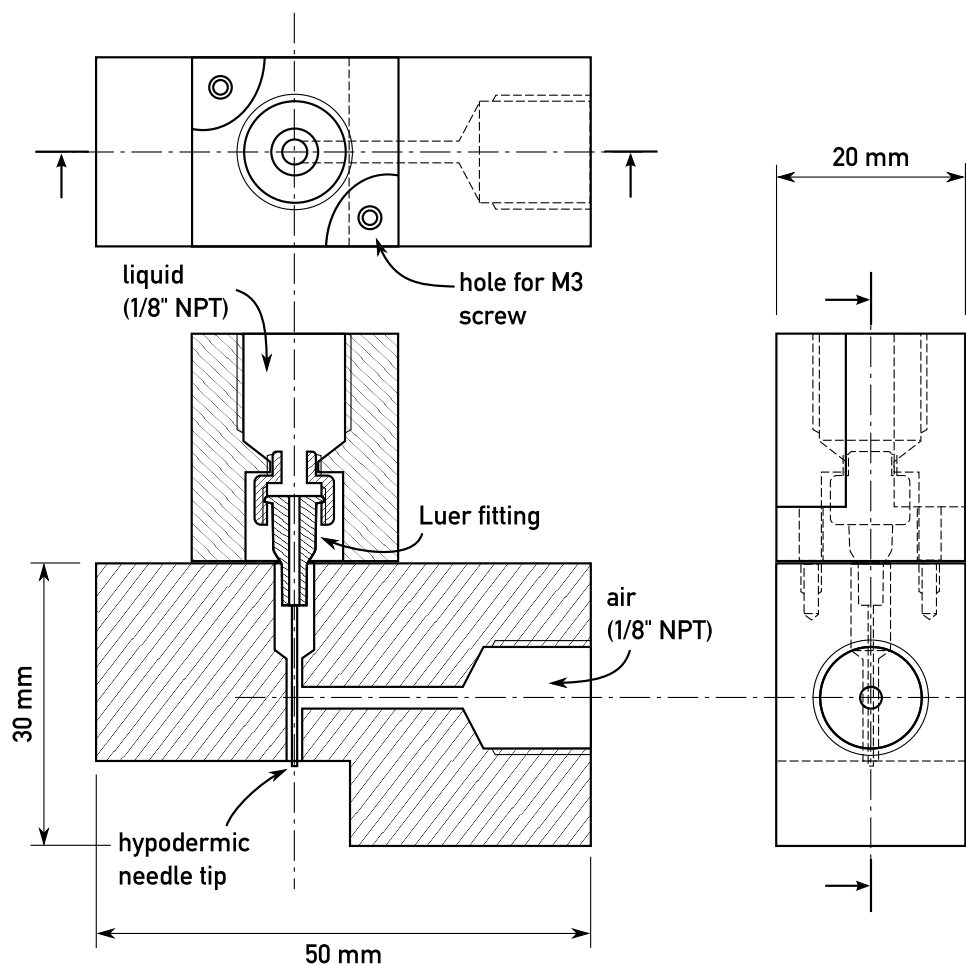


Figure 4.1: Schematic drawing of the coaxial-flow aerodynamic droplet generator, based on [?]. Top: top view, right: rear view (third angle projection). Sectional view illustrates operating principle.

4.2.1 Amirzadeh Goghari and Chandra design

We constructed a droplet generator based on the design by [?]. While both its construction from off-the-shelf parts and its operation are remarkably straightforward, it has two limitations:

- the duration of the air pulse is limited by the response time of the solenoid valve used. The shortest pulse we were able to reliable produce was on the order of a few milliseconds, which did not permit us to produce droplets smaller than a few hundred microns in diameter, and
- the head of water over the orifice must be kept very low to prevent leakage. As a result, the number of droplets that can be ejected is limited before the water needs to be replenished.

Owed to our lack of access to an automatic micropipette puller, the nozzles used in this experiment were not optimal, which likely contributed to our experience of frequent satellite droplets and liquid buildup at the nozzle tip.

4.2.2 Modified Yang design

A popular piezoelectric-based drop-on-demand design was proposed by [?]. It consists of a liquid-filled chamber, one wall of which is the underside of a piezoelectric disk—a brass disk coated with a circular piece of piezoelectric material, commonly found in electric buzzers.

To evaluate the performance of such a drop generator, we constructed several modifications of it, the final one of which is shown in Fig. 4.2. To make the chamber as flat as possible, minimizing the distance between piezoelectric disk and orifice, it has a depth of only about 2.5 mm, the thickness of a sheet of acrylic. A second sheet holds the disk in place, while a third sheet makes up the bottom wall of the chamber. Nozzle and inlet are glued directly into the bottom sheet.

To operate the droplet generator, water is fed through the inlet port until the chamber is filled and all air bubbles have escaped through the upward-facing nozzle. The generator is then turned so that the nozzle faces down and 30 ms pulses of about 30 V are delivered to the piezoelectric disk.

The greatest challenge faced was the accumulation of liquid on the nozzle surface, which quickly led to satellite droplets or thwarted droplet production altogether.

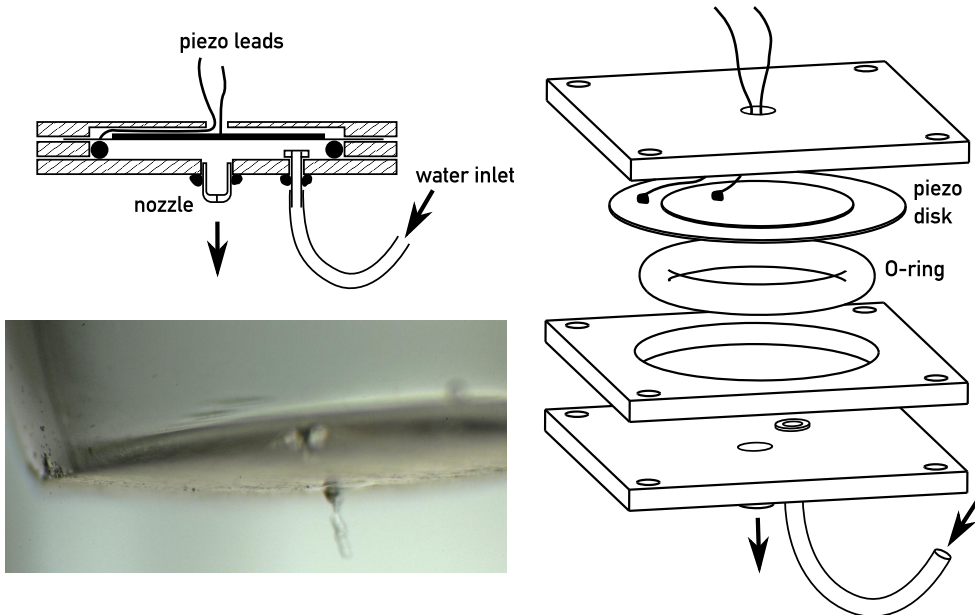


Figure 4.2: Top and right: schematic cross-section and exploded view of our piezoelectric droplet generator. Bottom left: photomicrograph of the nozzle tip ejecting a column of water (diameter $\approx 125 \mu\text{m}$), which is about to coalesce into a round droplet.

Again, capillaries drawn with an automatic pipette puller are likely more resistant to this effect.

4.2.3 Piezo-based drop generator

We tried building a Piezodropper from old piezoelectric elements squeezing glass capillaries (just like in the Ulmke paper), but two of the piezo elements were broken, and the third one had a capillary that clogged up repeatedly. We abandoned the approach before building a functioning droplet generator, although it seems attractive in practice. One downside is that the generation of amplified signals isn't straightforward – we used a soundcard connected to an amplifier to generate the signals.

4.3 Continuous-stream drop generation

There exist continuous-stream drop generators based on coaxial air flow [?] and on, but most continuous-stream drop generators are based on *Rayleigh breakup*, i.e. the disintegration of a disturbed liquid jet into droplets. The physics behind this phenomenon have been studied for almost two centuries [? ?] and are well-understood. When the jet disturbances are induced by carefully controlled mechanical vibrations at an appropriate frequency, the droplets will be of uniform size and evenly spaced.

This simple principle has been employed to generate droplets for fifty years, with orifices typically attached to either one of two vibrating mechanisms: an ordinary loudspeaker, first used by [?], or a piezoelectric element, as first proposed by [?] and popularized by Berglund and Liu's design [?].

4.3.1 Speaker-based drop generator

We used a big plastic underwater woofer, with a bendable metal strap taped to the cone. The end of the metal strap touched and vibrated the nozzle. At large droplet sizes, this is no problem at all, but once we get to about 1 kHz, the amplitude needs to go up considerably to yield a reliable breakup. In practice, this means that it gets very loud, jeopardizing the laboratory peace.

4.3.2 Hard-drive based drop generator

The accuracy of the hypodermic needle nozzle often isn't quite as good as that of e.g. photofabricated nozzles, as those have sharp edges. The round edges lead to variability in discharge coefficient (and mass flow), resulting in variance in drop volume [?]. Nevertheless, for the purpose of verifying the validity of measurements, it'll do.

Both speaker-based and piezo-based approaches have certain drawbacks: by design, a speaker vibrating at a fixed pitch produces an audible sound, jeopardizing the laboratory peace. Speakers are unshapely, difficult to fasten onto an experimental setup and their cones provide no robust structure to which any type of orifice could be attached. Piezoelectric elements cost more and are useful only when integrated with the orifice—precision machined droplet generators operating this way are commercially available, but unreasonably expensive in many situations. As a result, we felt compelled to consider alternative

sources of vibration that require a minimum effort to build and install using standard lab equipment, and chose the actuator mechanism found in every magnetic hard drive for the following properties:

Very low cost. With high-capacity and solid-state devices rapidly pushing older hard drives into obsolescence, it should be a simple matter to acquire a few decommissioned specimens for demolition. Hard drives come in two form factors—3.5 and 2.5 inches wide, respectively—and both can be used for the purposes of this paper.

Further, glass needle orifices fabricated for use with existing loudspeaker setups can be reused, and are easily produced by hand from heated borosilicate capillaries or using a micropipette puller. The process is illustrated in Fig. 4.3 and in-depth instructions are given by Lee[?]. Piezoelectric-based devices, on the other hand, need fitted orifices to produce a range of drop sizes.

Ease of construction and installation. Unlike loudspeakers, hard drives have a flat base plate which can be drilled into, allowing for easy installation on any experiment jig. Save for a drill and a saw, no machining tools are needed for the construction of the droplet generator.

High amplitudes without noise. Like piezoelectric elements, vibrating actuator arms are very quiet, enabling use at frequencies and amplitudes that would far exceed responsible levels on a speaker. In our experiments, the actuator responded to frequencies throughout our hearing range—i.e., up to 17 kHz—and likely well beyond, though we have not tested the full response range for any given amplitude.

As an added advantage over other designs, no amplification is needed. Below 100 Hz, amplitudes on the order of 0.5 cm are easily achieved (albeit they are of course not needed for droplet production) when a peak-to-peak voltage of 2 – 4 V is applied. The amplitude scales down with the inverse of the frequency, however, such that amplitudes are much smaller at typical operating frequencies (0.5 – 10 kHz). Nevertheless, the voltages required are well within the ability of any standard laboratory function generator, and can likely even be produced by many consumer-level computer sound cards.

Operating principle

Magnetic hard drives store data as sub-micron-sized patterns of oppositely magnetized dots on disks called *platters*. The read-write head is mounted at the tip of an arm that pivots across the platter surface while the platter spins. This setup allows the head to access the entire platter surface.

Fig. 4.4b illustrates schematically the design of a typical actuator arm assembly. The flat voice coil mounted on the surface is responsible for the arm's side-to-side movement: as it is positioned under a permanent magnet, the coil creates a sideward force when a current flows through its wires. By stopping or reversing the current the arm's motion is likewise stopped or reversed. Since a typical hard drive's platter spins at up to 7200 RPM, actuator arms must be able to move with extreme speed and precision. They are thus engineered to be very light yet stiff. These characteristics make a magnetic hard drive's actuator arm an ideal supplier of in-plane vibrations. Indeed, hard drive actuators are remarkable not for their operating principle but for their low cost; it is only the economics of mass manufacturing that has in recent years enabled these high-speed, lightweight precision mechanisms to become so widely available.

Construction

If possible, forgo multi-platter drives, as they are more cumbersome to disassemble and have bulky, complex actuator assemblies. The device shown in Fig. 4.4a is based on a single-platter drive.

Dismantle and cut. After removing the hard drive cover, remove the magnet holder, arm axis, arm, ribbon wires, circuit boards, and platters such that only the base plate remains. Now the corner of the base plate holding the actuator arm assembly can be cut out to yield the result shown in Fig. 4.4b. A band saw, jigsaw or powered hacksaw will be very useful, although



Figure 4.3: Above: assembly of nozzle from low-gauge hypodermic syringe (Luer fitting) and capillary. Below: nozzle tip fabrication, capillary from left to right: broken, sanded, heated in a flame (I.D. 200 μm), heated for longer (I.D. 25 μm , could be sanded down by about 200 μm), overheated (I.D. 0 μm).

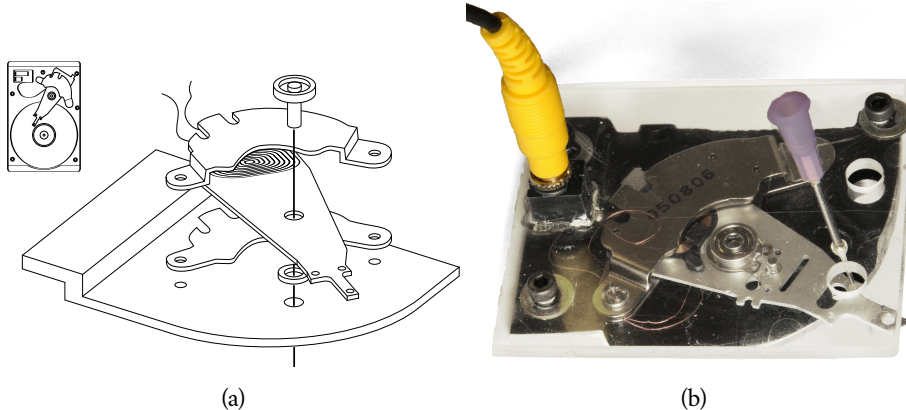


Figure 4.4: (a) top view of a hard drive and exploded view of the cut-out base plate, actuator arm, axis, and magnet assembly; (b) assembled droplet generator with cover plate and nozzle inserted through actuator arm.

not necessary. The goal is to allow the tip of the arm to protrude over the edge.

Expose coil leads. Next, remove the read/write head and all wiring leading to it, along with any connected I/O and servo circuitry. Be careful, however, not to tear off the two strands powering the voice coil. If they are integrated in a ribbon you wish to remove, ensure that exposed terminals remain onto which you can solder new leads.

Add protective cover. We recommend bolting on a cover plate, such as a small sheet of acrylic or polycarbonate, to protect the protruding arm from accidental bending. Drill a hole through the cover to allow the nozzle to be threaded through the arm. A severable connection from coil to function generator is preferable to a direct wire, if only because the voice coil leads are delicate and easily torn off. To this end, we epoxied an audio jack into the cover and soldered the voice coil leads to it from the bottom.

Operation

To use the droplet generator, simply insert a nozzle through a small hole at the tip of the actuator arm—typically at least one hole will already be present, but you may wish to drill more—and connect the voice coil leads to the output terminal of a function generator set to an initial peak-to-peak voltage of 1 V and a sinusoid frequency of about 50 Hz, which should cause weak but perceptible oscillations.

We used existing nozzles manufactured by hand from hypodermic needle stubs and heated glass capillaries (Fig. 4.3). We make no claim that this is the best approach to take, but we note that the interchangeability of nozzles with Luer fittings has proved very convenient in our application. How the nozzle can be held in place falls beyond the scope of this article; while we used an existing setup made from machined aluminum, a small lab stand and clamp should suffice to hold the male Luer fitting connecting the feed tube to the nozzle.

The nozzle must be supplied by an accurately calibrated syringe pump. It is convenient to integrate a large liquid reservoir (or tap water hose) via a T-valve between the pump and nozzle to permit quick topping up of the syringe. In such a setup ensure that the reservoir valve is shut closed before operation, since pressure fluctuations at the nozzle are the most common culprit for unstable jet breakup conditions.

As with other vibrating orifice droplet generators, it is crucial that stable conditions are established before any experiments can begin. First, confirm that the liquid is ejected in a single jet. Multiple jets can be due to a clogged orifice (a mixture of distilled water and CLR®, drawn back through a syringe, is an excellent remedy). Satellite droplets can also form secondary jets, in which case the oscillation frequency must be adjusted or the amplitude reduced. Satellite formation is easily detected by using a gentle air flow to deflect the jet—if the droplets are truly monodisperse, they will all deflect at the same angle.[?]

4.4 Determining the produced droplet size

With droplet generators based on Rayleigh breakup, such as the HDG, this is easy to do; just take the flow rate and divide by the number of droplets produced per second (which, under stable conditions, equals the vibration frequency as each instability turns into one droplet). If we assume perfect sphericity, we can convert this droplet volume into a diameter. After cancelling terms, the expression for D_d becomes

$$D_d = \sqrt[3]{\frac{6Q}{\pi f}} \quad (4.1)$$

The reliability of the underlying assumption has been verified photographically for several different nozzle orifice diameters and frequencies, some of which are given as part of the ILIDS calibration.

4.4.1 Photographing droplets

With drop-on-demand approaches, the diameter of the produced droplet is more difficult to predict, particularly since not the whole squeezing volume may result in ejected liquid (e.g. with the Chandra generator, it's just a small droplet). So to find out how big these droplets are (or just to verify the accuracy of Eq. (4.1)), we must resort to photographic means.

While there are different methods of photographing droplets, just taking pictures in front of a strobe light has worked well.

We used a scale placed next to the droplet stream, and then used a conversion between pixels to find the size. Of course, this method suffers from barrel distortion that inevitably happens, especially with a zoom lens. Figure X shows a typical droplet stream photo (at different sizes).

4.4.2 Droplet collisions

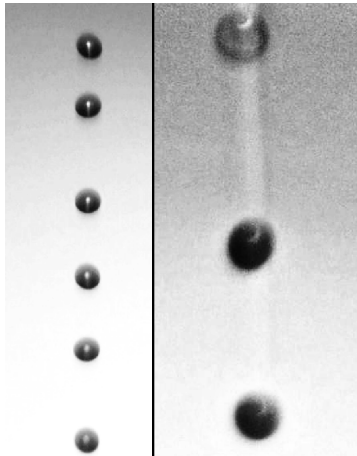


Figure 4.5: Photographs of different droplet sizes ($220\text{ }\mu\text{m}$ and $386\text{ }\mu\text{m}$, $f = 1.990\text{ kHz}$ and 1.065 kHz respectively) produced with the droplet generator shown in Fig. ???. Scales have been cropped out.

No droplet generation mechanism is perfect. Small fluctuations in flow rate, unwanted harmonic vibrations and air turbulence can cause disturbances in the stream of evenly spaced droplets – the smaller the droplets, the more often this happens. Occasionally, this will lead to the collision of two droplets some distance away from the orifice.

When two drops of diameter D_d collide, the diameter of the new droplet equals

$$D_{d+d} = 2 \sqrt[3]{2 \left(\frac{D_d}{2} \right)^3} = \sqrt[3]{2} D_d \approx 1.26 D_d. \quad (4.2)$$

Indeed, secondary peaks will often appear in diameter histograms at precisely 126% of the peak diameter. As long as the underlying phenomenon is understood and kept under control, these secondary peaks should be no cause for concern during the calibration. Typically, photographs will confirm that a

few droplets go astray and collide with others. Since the “real” diameter peaks are easily discerned, the secondary peaks can simply be ignored.

ILIDS

Interferometric Laser Imaging for Droplet Sizing (ILIDS), also known as Interferometric Particle Imaging (IPI) and MSI (Mie Scattering Imaging) is an optical droplet sizing method in which a spray is illuminated by a sheet of laser light and the scattered light is imaged laterally. The laser light is both reflected and refracted by the droplets, such that each droplet produces a pair of apparent “glare points”. When seen through a lens away from the focal plane, each pair of glare points—being sources of coherent monochromatic light—appears as an interference pattern which, after falling through a circular aperture, casts an image that is a circular disk of fringes. The spatial frequency of the fringes is (to a very close approximation) linearly related to the particle size. The phenomenon was first described by [1] and later in greater detail by [2]. Turnkey ILIDS setups for spray characterization are now widely available, comprising typically a pulsed Nd:YAG-laser, one or two CCD cameras, a timing circuit, and a piece of image processing software.

5.1 Operating principle

The number of fringes N_{fr} appearing in the image has a simple linear relationship to the droplet diametre D_d :

$$N_{\text{fr}} = \kappa D_d, \quad (5.1)$$

where κ is a constant derived from the optical configuration:

$$\kappa = \frac{\arcsin\left(\frac{D_d}{2z}\right)}{\lambda} \left(\cos \frac{\varphi}{2} - \frac{m \sin \frac{\varphi}{2}}{\sqrt{m^2 + 1 - 2m \cos \frac{\varphi}{2}}} \right). \quad (5.2)$$

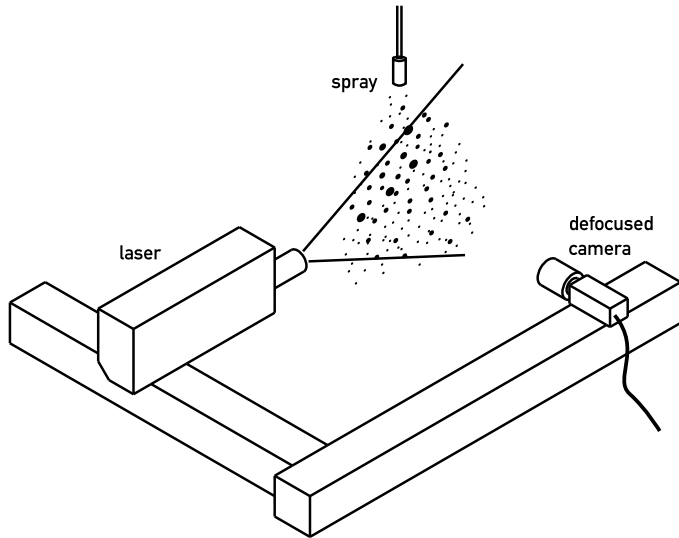


Figure 5.1: Perpendicular ($\varphi = 90^\circ$), single-camera ILIDS setup

In the above expression D_a is the aperture diametre, z is the distance of the lens to the laser sheet, φ is the off-axis angle (90 degrees in most setups, including ours), and m is the relative refractive index of the droplets (1.333 for water in air).

As a consequence of geometrical optics, the distance s_x (in pixels) between two adjacent fringes has a linear relationship with the defocussing distance Δz , where M is the magnification, $d_{p,x}$ is the physical size of a camera sensor pixel, and $\Delta\vartheta$ is the angle subtended by two adjacent fringes entering the lens [?]:

$$s_x = \frac{\Delta\vartheta\Delta z}{Md_{p,x}} \quad (5.3)$$

Of course, equation (5.3) is only meaningful where $\Delta z \gg 0$. When the image is brought into focus ($z \approx 0$), fringes will give way to a sharp image of the glare points.¹ Of course, if the pixel density is too low to resolve both glare points, a single bright spot will appear.

¹To be exact, diffraction will cause every point to be imaged as an Airy disk, but we shall neglect this effect here.

5.1.1 Influence of the scattering angle φ

The scattering angle φ , illustrated in Fig. 5.2, determines the relative contribution of different scattering orders of light to the imaged fringe pattern. Both geometric optics [?] and Mie theory provide methods to compute the total scattered intensity for a given φ and m ; some examples can be found in [?] and [?]. The geometric analysis approach is not valid beyond $\varphi > 70^\circ$, as the first-order scattered beam ($p = 1$) is not visible from this angle [?].

While authors have identified several forward angles as optimal for their applications, e.g. $\varphi = 45^\circ$ [?] or $\varphi = 66^\circ$ [?], such configurations inevitably result in a variation in z , and therefore defocusing, across the image unless the camera itself is angled with respect to the lens to correct for this aberration (the so-called *Scheimpflug condition*). Since the latter approach requires specialized optical equipment, $\varphi = 90^\circ$ is used in many setups, including the one in this paper.

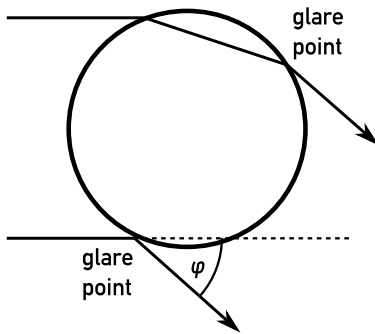


Figure 5.2: Reflected and first-order refracted light rays, producing two glare points when viewed from an angle φ .

5.1.2 Optical limits on fringe detection

Optics impose theoretical and practical size limits on the droplets to be measured. We will outline them in the following paragraphs; the reader is referred to [?] for a more detailed analysis.

Nyquist criterion for the fringe density. The Nyquist criterion requires that for the camera to be able to resolve a pair of neighbouring fringes, their images must be at least two pixels apart. This can easily be achieved by a sufficient defocusing the lens, which widens the fringe image, increasing the number of pixels covered by each fringe. The lens mechanics permitting, any arbitrarily large droplet can thus be measured after a quick adjustment. In theory, this correction is effective until the defocused droplet image is too large for the CCD sensor, and fringes are cut off. In practice, overlap and noise (see below) will cause significant problems long before the image can be defocussed beyond the sensor edges.

Signal-to-noise ratio. Image noise is a significant source of trouble in ILIDS analysis. Indeed, many droplet images must be discarded as data sources because they are too weak compared to the noise. Small droplets suffer from this more than larger ones because they scatter less light,² but the problem also occurs with deeply out-of-focus images of very large droplets, as dilated droplet images spread the same amount of light over a greater area on the camera sensor. As a result, they are darker on average than less defocused images.

Minimum droplet size. [?] argue that the smallest measurable droplet is one that produces exactly one fringe falling through the aperture. We may speculate that, at least in theory, the fringe frequency should be measurable even if only a partial fringe is shown. This would require its image to be sufficiently zero-padded before the Fourier transform is applied to it. In practice, however, the intensity of scattered light typically drops below an acceptable level well before the fringes become too large, and noise (see above) will become the overwhelming problem.

Deviation from actual Mie scattering for small droplet sizes. ILIDS users should also be aware that the assumptions of geometric optics that underlie (5.2) do not hold for small droplets. [?] found that for isoctane droplets ($m = 1.39$) below $10 \mu\text{m}$, geometric optics yield a fringe spacing value about 14% higher than that predicted by exact Mie scattering simulations at $\lambda = 532 \text{ nm}$. While the deviation quickly vanishes for larger droplets, it is nevertheless noteworthy in the context of potential error sources.

Overlapping droplet images. The ability to image a whole 2D field of droplets all at once is ILIDS' strongest selling point, yet also its curse. When droplets are spaced too closely and the lens is sufficiently defocused, the defocused disk images overlap and it becomes difficult to determine the fringe counts corresponding to individual droplets. [?] provide a statistical estimate on the fraction of overlapping disks (overlap coefficient).

²The scattered intensity grows with the cross-section of the droplet

5.2 Types of ILIDS setups

5.2.1 Standard ILIDS

The most simple ILIDS configuration, as shown in Fig. 5.1, consists of a single digital camera with a defocused objective lens, placed at a right angle to the laser sheet. The lens aperture is (approximately) circular and typically completely open to permit as much light as possible to fall on the sensor area.

Both camera and laser are connected to a computer via a timing circuit, and both can be triggered simultaneously by software installed on the computer. Commercial ILIDS vendors provide the timing circuitry and the software, which typically integrates a collection of image processing algorithms that can be used to analyze the captured images immediately.

The core problem with all ILIDS setups is the determination of z and d_a in (5.2). We will discuss calibration of ILIDS systems in greater detail in Section ?? calibration.

Images taken in this configuration are very susceptible to excessive disk overlap.

Therefore, measures have been developed to sidestep overlap almost entirely or to deal with it during the image processing stage. These modifications will be described in the next sections.

5.2.2 ILIDS with optical compression

This problem is never more apparent than in efforts to calibrate the system using a vibrating orifice droplet generator, as the droplets produced thereby are spaced very closely and produce heavily overlapping defocussed images. Fortunately, there exists a simple and reliable technique to deal with this problem: a slit aperture, installed directly in front of the lens, masks the defocussed droplet images such that only a thin strip across their center passes through the lens. The effect is shown in Fig. 5.3.

Arguably the most popular way to reduce the amount of overlap is the use of optical compression techniques, whether by means of a slit aperture [?] or a cylindrical lens [? ?]. However, some techniques (e.g. Global Phase-Doppler [?]) and intensity-analyzing methods [?]) or use cases (e.g. very low signal-to-noise ratios) require the full disk image to be available. In these cases, the standard approach is to identify the location and outline of each disk image, such that the fringe analysis can either be limited to non-overlapping

regions or be otherwise modified to take overlapping fringes into account.

Naturally, equations (5.2) and (5.3) still hold. Also mention that this can be used in con-

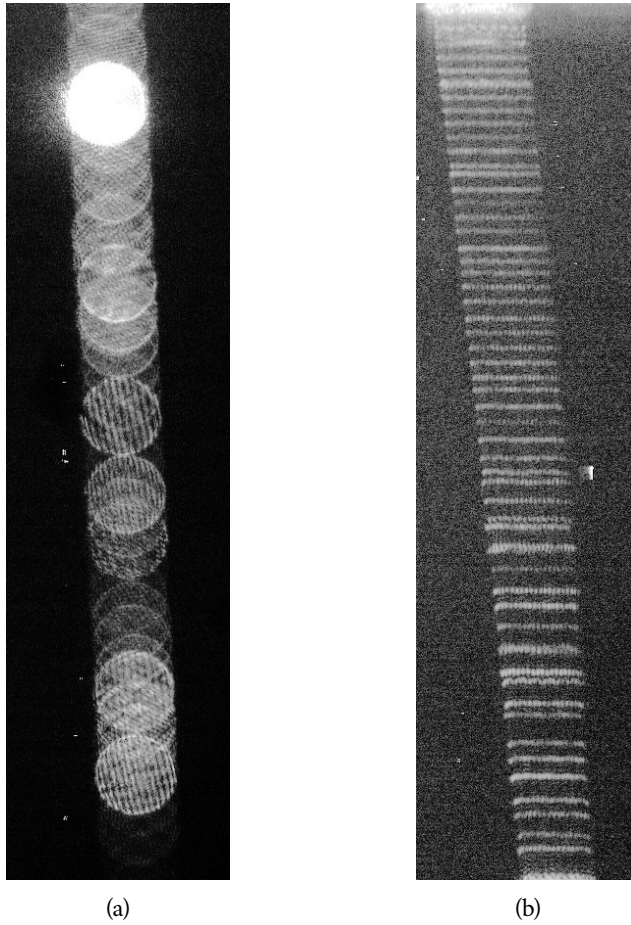


Figure 5.3: Before (a) and after (b) installing the slit aperture. The aperture stop pares off the top and bottom halves of the defocussed circles, leaving only a narrow center string in the middle.

jecture with an additional, focused camera, to capture things like speed (PIV), evaporation (PLIF), etc. Why we don't need it.

Extracting the fringe counts from such an image is straightforward. First, we correlate the image with that of a single, solid bright rectangle which shares the approximate dimensions of a typical strip in the image. This operation yields intensity peaks centered over our regions of interest. We remove closely adjacent peaks, as they may represent questionable

or overlapping strips. Compared to the sheer number of correctly identified strips, the number of legitimate data points lost this way is negligible. Fig. 5.4 shows the result of such an attempt at identifying the strips.

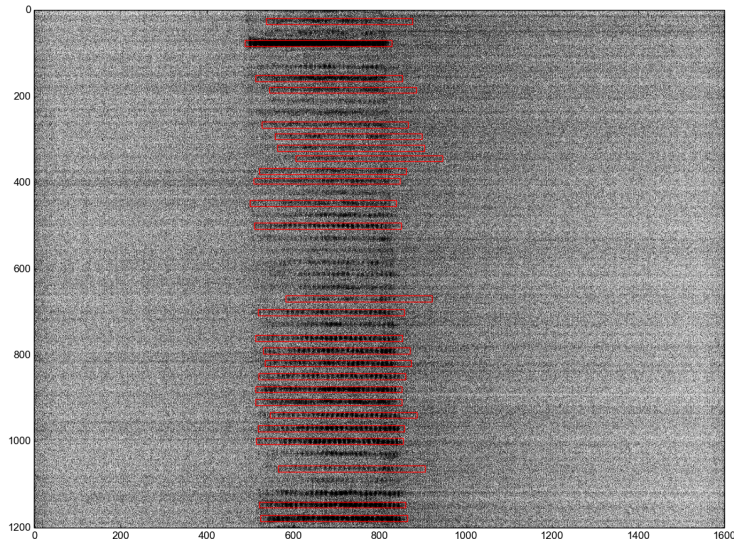


Figure 5.4: The image is correlated with that of a solid bright rectangle, which results in peaks that approximately coincide with the centers of the strips. Here, the original photo is shown with rectangles drawn centered at said peaks.

To find the number of fringes within the strip, we cannot rely on counting the number of dark/bright variations directly, as some of them may be lost in the noise. The spatial frequency of the peaks, however, taken together with the known and constant horizontal width of the strips, will produce a reliable fringe count. In the next step, our algorithm therefore applies the Fourier transform to each region of interest. To improve the accuracy of the method, three steps are performed before the Fourier transform is taken:

1. a weak (3×3) Gaussian blur is applied to the region (optional);
2. a Hanning window is applied to the region – both horizontally and vertically. This reduces the “sinc ringing” effect encountered when taking the Fourier transform of finite signals;
3. the region is padded with zeros in all directions to yield a larger input to the Fourier transform. In our application, the windowed and padded strip images had dimen-

sions of 1024×1024 pixels. Zero-padding increases the granularity of the frequency spectrum, which can help with the correct identification of the peak frequency.

Fig. 5.5 shows the windowed appearance of one such region of interest (although it does not show the padded input to the Fourier transform due to space constraints). The Fourier transform yields a frequency power spectrum in two dimensions, although we are primarily interested in the frequency peak in the horizontal direction (i.e. along $y = 0$). In order to minimize the misidentification of dominant frequencies,

1. we clip the spectrum to a band of reasonable frequencies. This is necessary because
 - a) $1/f$ -noise causes very low frequencies to dominate in power, although they are of no interest to us, and b) graininess in the original photo can sometimes result in meritless high-frequency peaks;
2. we apply a Gaussian blur to the 2D spectrum to remove outliers in the spectrum;
3. we discard all regions in which the peak frequency's power does not exceed a certain value;
4. we discard all regions in which the *prominence* of the peak frequency's power (i.e. its proportion to the mean power) does not exceed a certain value (this step is optional).

The bottom two elements in Fig. 5.5 illustrate the effect of these steps.

Finally, the peak frequency f_{peak} is converted into a fringe count by re-scaling it from the padded size D_{padded} ($= 1024$ pixels) to the width of the strip (which, in the context of IPI measurements, should equal the diameter D_i of the defocussed droplet image):

$$N_{\text{fr}} = f_{\text{peak}} \frac{D_i}{D_{\text{padded}}} \quad (5.4)$$

While the above algorithm will generally give a good estimate of the fringe count for a given defocussed droplet image, it cannot know whether the entire center portion of the image has indeed passed the slit aperture. It is conceivable, after all, that the slit aperture was not perfectly centered on the lens entrance, or that the slit aperture was shorter than the diameter of the lens entrance. Fig. 5.6 illustrates how the slit aperture can cause the defocussed image to appear smaller than it is. The reduced

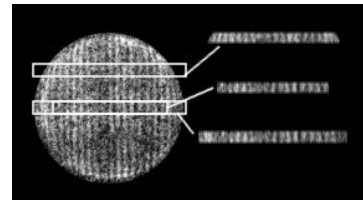


Figure 5.6: Only a slit aperture centered on the lens and extending across the entire lens entrance will preserve all fringes

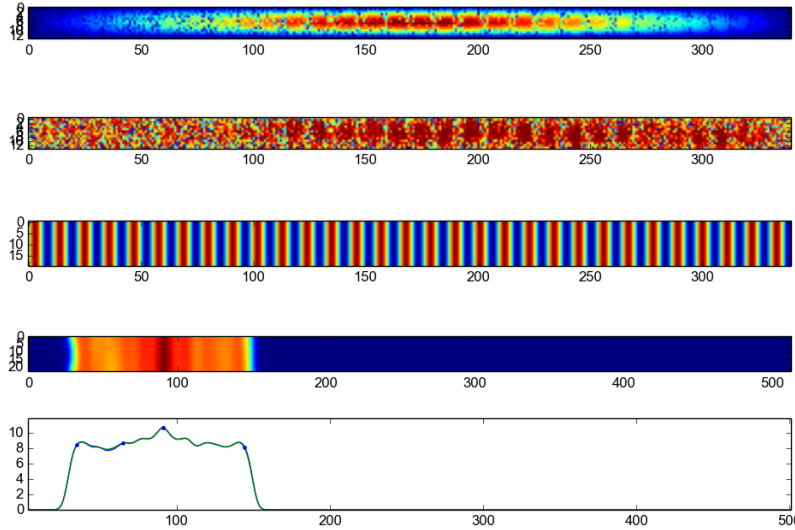


Figure 5.5: From top to bottom: windowed region of interest; original (unwindowed) region of interest; sine wave representing the identified peak frequency; clipped and lowpass-filtered 2D frequency spectrum showing a distinct peak at about 90 oscillations across the image width of 1024 pixels; 1D plot of the frequency spectrum, with peak identified at $f = 91.0$.

value for D_i , manually entered in equation (5.4), will result in droplets being reported as smaller than they are in reality.

As noted above, ILIDS with optical compression can be used with an additional, focused camera behind a beam splitter, as shown in Fig. 5.7.³ The latter may provide e.g. PIV images for a velocity analysis or LIF images for evaporation studies. This was demonstrated by [?] and [?]. However, such setups suffer from *center discrepancies*. Section 5.5 documents how such center discrepancies can be dealt with.

5.2.3 Additional focused image for disk detection

As described above, running a simple frequency analysis on bright regions in an ILIDS image is futile when two of the fringe disks overlap, as it is not clear how many droplets are associated with the region and where their disks infringe. While optical compression provides a very good solution to this problem, it is not always applicable: some techniques

³Alternatively, the two cameras may image the spray from different angles, e.g. as demonstrated by [?], although this complicates the setup as the Scheimpflug condition must be fulfilled.

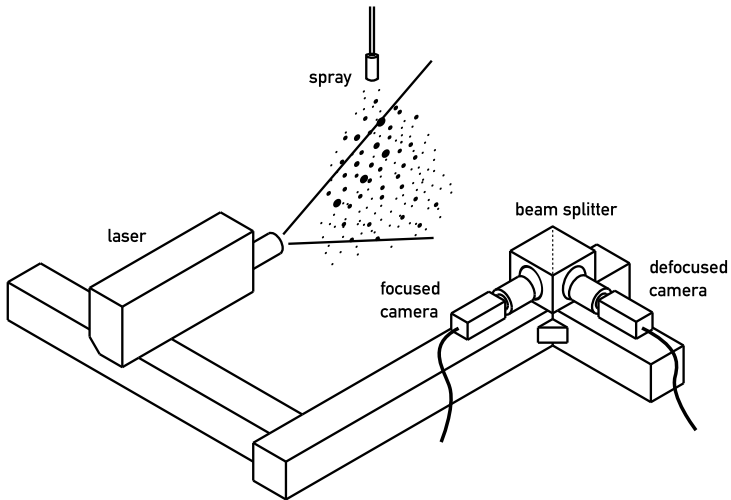


Figure 5.7: Perpendicular ($\varphi = 90^\circ$), double-camera ILIDS setup

(e.g. Global Phase-Doppler [?] and intensity-analyzing methods [?]) or use cases (e.g. very low signal-to-noise ratios) require the full disk image to be available. In these cases, the standard approach is to identify the location and outline of each disk image, such that the fringe analysis can either be limited to non-overlapping regions or be otherwise modified to take overlapping fringes into account. Additionally, once disk centers are found, the software can apply Hanning windows to the disks as well as ignore disk pairs that are too close.⁴

To identify the location of overlapping disks in the image, an additional camera is introduced to capture a focused image of the spray simultaneously with the defocused ILIDS camera. The setup is identical to that shown in Fig. 5.7. The intensity peaks in the focused image are then taken to be the droplet positions (i.e. disk centers) in the defocused image.

The problem with this, as with all multi-camera setups, are center discrepancies. We show how to overcome that in Section 5.4.

⁴The latter is an effective control mechanism, but is liable to skew the representativeness of the sample because small, dispersed satellites outside of the main flow are most likely to be validated.

5.3 Calibrating the slit method

What matters is the Numerical Aperture (NA), which is (the sine of half of) the collection angle. When we have a simple lens, we can calculate this as

$$\text{NA} = \sin \frac{d_a}{2z} \quad (5.5)$$

The Dantec manual suggests using the distance from light sheet to front of the lens for z , and the ratio of min focal length and max f-number to find d_a . This, however, does not result in an accurate value for the collection angle with all lenses.

We are assuming, then, that the effective aperture (the entrance pupil) always stays constant throughout the focussing range of the lens. This is not necessarily the case, as there are lenses which change both the physical and the virtual size of the aperture when focussing.

Here is where I make the claim that it is impossible to determine the actual exact value for the numerical aperture of the lens. Similarly, it can be quite difficult to determine the accurate distance from light sheet to lens aperture (even though the latter measurement is more forgiving, since the distances are far greater).

Taking into account the sources of errors explained in the sections above, it is advisable to run a few calibration tests with droplets of different sizes before employing the IPI technique for real spray measurements. Recall that, if we ignore the Mie error (Section ??), the relationship between fringe count and droplet diameter is linear with a constant of proportionality χ (see equation (5.2)). The aim of our calibration, then, is to determine the value of χ from experiment – the premise being that we cannot be certain of the values of D_a , z , and possibly not even m and φ (although the latter can usually be ascertained to a sufficient degree of accuracy).

5.3.1 A sample calibration of the slit aperture method

Using the droplet generator described in Section 4 and the IPI configuration described in Section 5.2, we produced and measured monodisperse droplets of many different diameters. The droplet diameters were determined both mathematically and photographically, as described in Section ???. Out of over 30 sets of IPI measurements we selected six sets that exhibited both strong uniformity and high photographic quality:

| Set | Flow rate | Frequency | D_d , predicted | D_d , from photo | \hat{N}_{fr} |
|-----|------------|-----------|-------------------|--------------------|----------------|
| FA | 20.8 ml/h | 5395 Hz | 127 μm | 126 μm | 9.71 |
| FB | 39.7 ml/h | 1990 Hz | 220 μm | 226 μm | 16.71 |
| FC | 79.4 ml/h | 1565 Hz | 299 μm | 291 μm | 22.92 |
| FD | 94.3 ml/h | 1067 Hz | 361 μm | 367 μm | 27.26 |
| FE | 114.1 ml/h | 1065 Hz | 384 μm | 384 μm | 29.89 |
| FF | 175.2 ml/h | 1038 Hz | 447 μm | 454 μm | 34.56 |

Table 5.1: Six sets of calibration data taken with the setup described in Section 5.2

The values for \hat{N}_{fr} , the peak fringe count, are based on the histograms (see Fig. 5.8) showing the distribution of fringe counts within each dataset. These fringe counts are of course found by the algorithm described in Section ??.

It is worthwhile to point out some apparent idiosyncrasies in the histograms of datasets FB and FC. Their peak fringe counts are 16.71 and 22.92, but there are secondary peaks at about 21 and 29 fringes, respectively. The latter are explained by the collision of droplets as discussed in Section 4.4.2, and are ignored for the purposes of calibration.

The close agreement of the droplet diameters found from photographs with those predicted by (??) reassures us that we can use the predicted D_d for further analysis.

At this point, we can least-squares-fit the linear relationship (5.2) to the primary peaks \hat{N}_{fr} and the known droplet diameters D_d to find \hat{x} :

$$\hat{x} = \frac{\sum_i D_{d,i} \hat{N}_{fr,i}}{\sum_i D_{d,i}^2} \quad (5.6)$$

Note that instead of the standard least squares regression we here use a simplified formula to force the trend line through the origin. This choice should not be made lightly, since it will usually cause the residuals to have a non-zero mean. In this case, however, we believe it to be justified to require that $D_d = 0$ for $N_{fr} = 0$.

Based on the values in Table 5.1, we thus arrive at a value of $\hat{x} = 76808.1$ with an R^2 -value of 99.98%.

Fig. 5.9 illustrates the good agreement on x between all datasets. Considering the sheer number of error sources – from the unavoidable non-uniformity of the generated droplets to the uncertainty that comes with taking the Fourier transform of a noisy image – the calibration results documented here are a testament to the practical robustness of the method.

It must be remembered, of course, that the peak fringe count values \hat{N}_{fr} forming the ba-

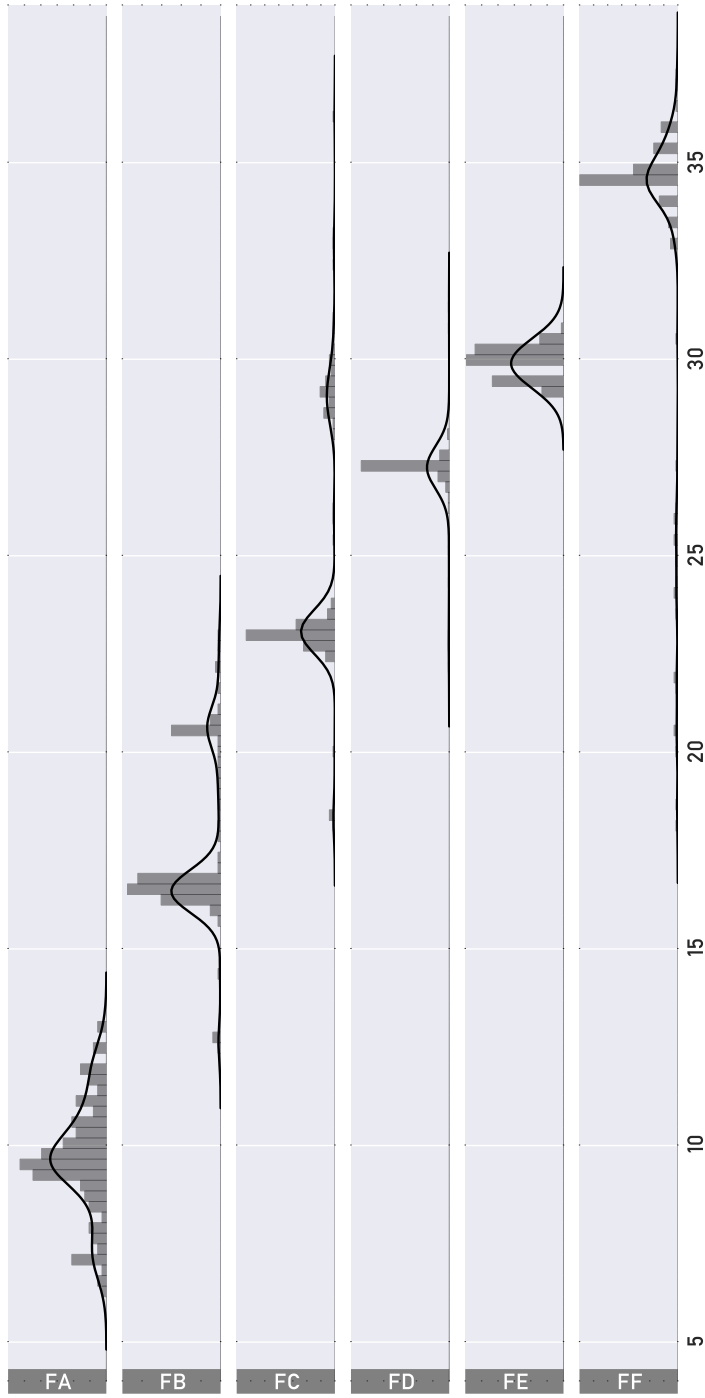


Figure 5.8: Normalized distributions of measured fringe counts N_{fr} for the six datasets listed in Table 5.1. Solid lines are Gaussian kernel density estimates with $h = 0.5$.

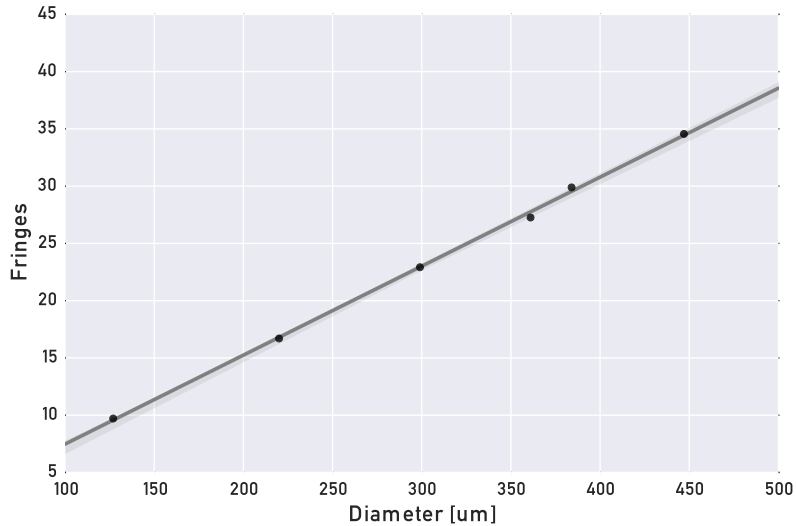


Figure 5.9: Scatterplot of Table 5.1 showing the peak fringe counts \hat{N}_{fr} for each predicted droplet diameter D_d

sis of our calculation are taken from the peaks of Gaussians fitted to the raw fringe count histograms (see Fig. 5.8). In other words, it is our assumption that all droplets from a given dataset produce fringe counts that are normally distributed around their respective \hat{N}_{fr} . The histogram to dataset FA shows a much higher deviation than the others – this may be due to genuine variance in the generated droplet diameters or to difficulty in processing comparatively weak images with low fringe counts. It seems likely that both effects contribute.

We can compare the empirically determined value \hat{x} with the mathematical result obtained from (5.2). Substituting $\lambda = 532 \text{ nm}$, $m = 1.3324$ and $\varphi = 90^\circ$, we conclude that

$$\frac{D_a}{z} = 2 \sin \left(\frac{\hat{x}\lambda}{\cos \frac{\varphi}{2} - \frac{m \sin \frac{\varphi}{2}}{\sqrt{m^2 + 1 - 2m \cos \frac{\varphi}{2}}}} \right) = 2 \sin(3.11982 \cdot 10^{-7} \hat{x}) \quad (5.7)$$

so for $\hat{x} = 76808.1$, $\frac{D_a}{z} = 0.047921$. Recall that this quotient is a measure of the collection angle and closely related to the numerical aperture $\text{NA} = \sin \frac{D_a}{2z}$. If needed, we can now use this result to compute the input parameters D_a and z in the DantecStudio IPI software:

given, for instance, $z = 45.0$ cm, we can obtain the entrance pupil diameter as

$$0.047921 \cdot 450 \text{ mm} = 2.156 \text{ mm} \quad (5.8)$$

5.4 Removing center discrepancies with keypoint registration

As mentioned above, to allow both cameras to image the same physical region in the spray, they are either placed behind a beamsplitter at a right angle to the light sheet, or placed separately at different angles. The latter approach makes for a more difficult setup, since Scheimpflug's rule demands that the camera must be tilted with respect to the objective lens, but it gives the user the freedom to choose the highest-intensity scattering angle.

In any of the above cases, the use of two cameras requires that their images be mapped onto one another. This is commonly achieved by means of a camera calibration procedure, in which a target pattern (e.g. as in Fig. 5.10) of known dimensions is photographed by each camera. A pattern recognition algorithm then determines the object-to-image mappings for each camera:

$$\begin{bmatrix} x' \\ y' \\ z' \\ r' \end{bmatrix} = \begin{bmatrix} S_x & A_{yx} & A_{zx} & T_x \\ A_{xy} & S_y & A_{zy} & T_y \\ A_{xz} & A_{xy} & S_z & T_z \\ P_x & P_y & P_z & S_0 \end{bmatrix} \begin{bmatrix} x \\ y \\ z \\ 1 \end{bmatrix}. \quad (5.9)$$

In our case, Dantec supplied a *standard dot target*, a white $10 \times 10 \text{ cm}^2$ plate engraved with a pattern of black dots. The plate is to be mounted such that its surface coincides perfectly with the laser sheet.

In practice, $P_{x,y,z} = 0$ and $S_0 = 1$ is assumed, such that the mapping is affine. The z -components (third row/column) are further assumed to be zero, such that a 3×3 matrix suffices for the purposes of this discussion:

$$\begin{bmatrix} x' \\ y' \\ r' \end{bmatrix} = \begin{bmatrix} S_x & A_{yx} & T_x \\ A_{xy} & S_y & T_y \\ P_x & P_y & S_0 \end{bmatrix} \begin{bmatrix} x \\ y \\ 1 \end{bmatrix}. \quad (5.10)$$

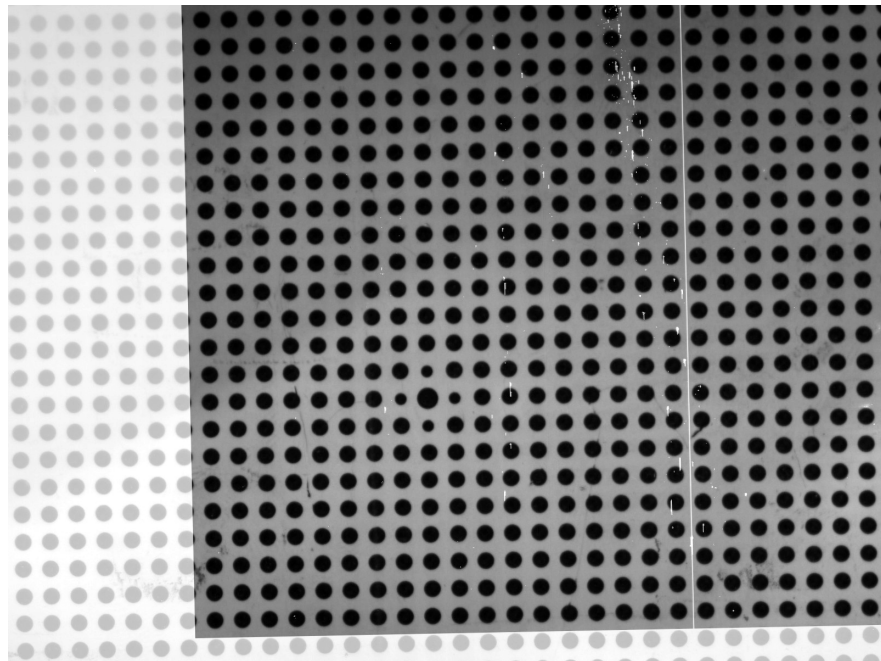


Figure 5.10: Homography \mathbf{H} applied to target pattern image captured by the focused camera and superimposed on the image captured by the defocused camera (here, both cameras were in focus for the calibration only).

The calibration algorithm thus finds the camera matrices \mathbf{P}_{foc} and \mathbf{P}_{def} mapping the object coordinates \mathbf{x} onto the two camera images \mathbf{x}'_{foc} and \mathbf{x}'_{def} (the respective subscripts shall hence designate the focused and defocused cameras):

$$\mathbf{x}'_{\text{foc}} = \mathbf{P}_{\text{foc}} \mathbf{x} \quad (5.11)$$

$$\mathbf{x}'_{\text{def}} = \mathbf{P}_{\text{def}} \mathbf{x}. \quad (5.12)$$

It follows that the quotient of the two matrices, also known as the homography

$$\mathbf{H} = \mathbf{P}_{\text{def}} \mathbf{P}_{\text{foc}}^{-1} \quad (5.13)$$

can be used to map the focused image onto the defocused image, as shown in Fig. 5.10:

$$\mathbf{H} \mathbf{x}'_{\text{foc}} = \mathbf{x}'_{\text{def}}. \quad (5.14)$$

Unfortunately, the calibration procedure itself introduces an unwanted distortion: to capture a viable photo of the target pattern, the defocused camera must be temporarily brought into focus, as was done in Fig. 5.10. This is not mentioned e.g. in the application manual of Dantec's IPI system, but is a practical necessity. Bringing a camera out of focus not only introduces a blur, it also scales the image extents. Fig. 5.11, adapted from [?], shows schematically how this effect creates “center discrepancies”. Since the extents of the defocused image are either smaller or larger than those of the focused image, depending on the direction of defocusing, all droplet images are projected either closer to or farther away from the image center. The discrepancy is worst for droplets far away from the image center. As a result, the centers of objects in simultaneously captured focused and defocused images no longer align (Fig. 5.12), and the calibration procedure becomes self-defeating.

While this error is easy to account for in the ideal case of right angles and perfect alignments (simply rescaling the image would solve the problem) the situation becomes more difficult in practice when the target pattern is no longer parallel to the camera sensor (intentionally or accidentally) or when cylindrical lenses are used to add optical compression. In fact, there is no guarantee that affine mappings are sufficient in the general case.

Surprisingly, only Hardalupas *et al.* [? ?] have hitherto published a discussion of this effect, and the only previous mention known to the authors is in [?], who dismissed it as a “positioning error”.

Hardalupas *et al.* identified the centers of particles in both PIV (focused) and ILIDS

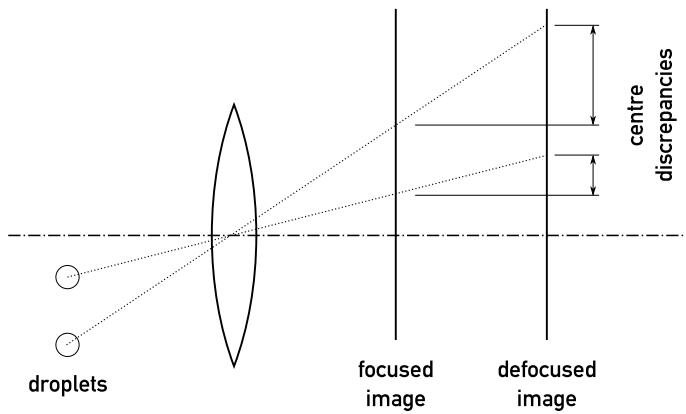


Figure 5.11: Schematic showing the source of center discrepancies in the case of parallel image and object planes

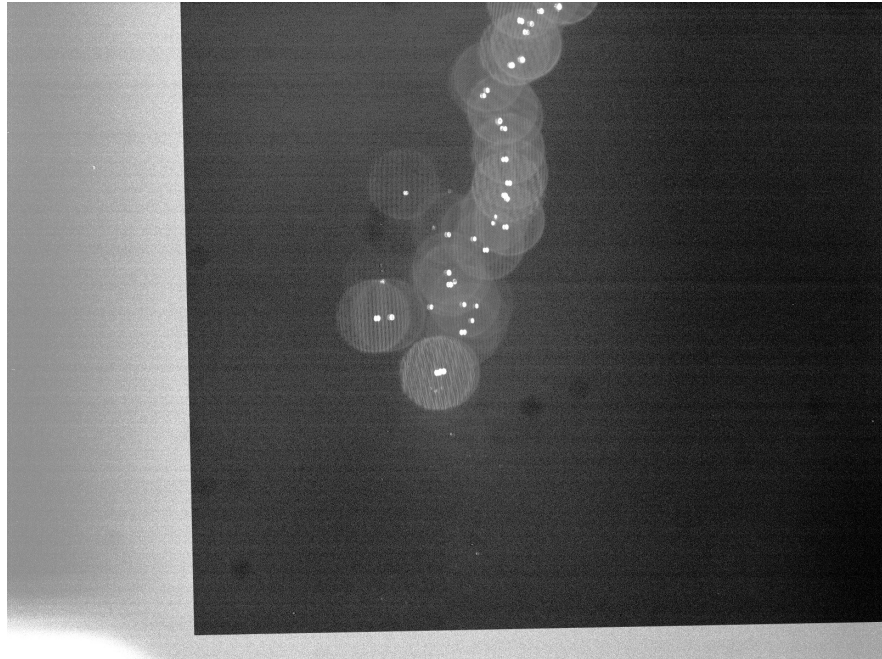


Figure 5.12: Focused camera image, after applying homography \mathbf{H} derived from the calibration images, is superimposed onto defocused camera image of droplets. Discrepancies between object centers grow towards the edge of the image.

(defocused) images. They then empirically estimated the magnitude of the center discrepancy effect along the vertical axis, which enabled them to improve the accuracy of their nearest-neighbour-based droplet image matching algorithm.

We found that algorithms developed by the computer vision community in recent years can obviate the need for calibration entirely. Instead, we can use visual correspondences between the focused and defocused images to find the mapping between them directly. To that end, we first provide in Section 5.4.1 a brief overview over popular methods in the field of automated (linear) *registration*, i.e. the art of finding a *homography* (geometric mapping) between two *epipolar images* (images of the same object, taken from different positions and angles). Section ?? documents our approach in greater detail and shows the result of a successful recalibration.

5.4.1 Review of image registration techniques

Given two identical images that have been rotated, shifted or even scaled with respect to one another, the applied transformation can theoretically be found by means of a brute-force search. This method is not feasible in practice, not only because of its enormous computational complexity (there are no gradients to guide the search) but also because of its inability to deal with noise, focal blur, perspective changes and other nonlinearities introduced by the photographic process. Conversely, normalized cross-correlation measures between images, as commonly used in PIV, are unaffected by noise but not invariant to rotation and scale and therefore not generally practical. The standard approach to image registration is therefore a three-step process. First, *keypoints*, i.e. “interesting” points in the images are found by a keypoint detection algorithm. Then, a small image patch at every keypoint is extracted and converted into a *feature vector*, a set of numbers providing a very general description of the image patch that accounts for scale, rotation, blur, contrast, etc. Finally, matches between similar feature vectors from the two images are found, outliers are removed, and the homography is calculated.

However, the results of a keypoint detection algorithm must be as repeatable as possible, i.e. the same set keypoints should be found in both images regardless of their relative position, rotation, scale, etc. For instance, the Harris corner detector [?], one of the earliest keypoint detectors, is sensitive to scale and thus often unusable.

The recent decade has seen a rapidly growing collection of proposed keypoint detectors, beginning with SIFT [?], SURF [?] and BRISK [?], all of which include keypoint ex-

tractors, to CENSURE [?], optimized for speed, and FAST [?], which incorporates machine learning methods. Finally, the recent publication of ORB [?] includes a rotation-aware version of FAST used in this paper. Many more have been developed but are not included here for brevity's sake.

Keypoint extractors (sometimes called *descriptors*) are often optimized for and therefore included with keypoint detectors, as in the instances mentioned above. Some however are standalone algorithms, such as BRIEF [?].

It is straightforward to find matching keypoints by searching for pairs with the smallest arithmetic distance between their feature vectors (e.g. using the L^2 norm). This nearest-neighbour search can be done exhaustively in linear time to find the optimal matching, but many faster, if approximate, search methods exist. We should note FLANN [?], a publicly available collection of such implementations which includes a fully automatic parameter selection heuristic.

Finally, the homography, assuming one exists, can be derived from the set of matched keypoint coordinate pairs. Since many of the found matches will be wrong, it is of essence to use a robust estimator, i.e. a type of regression model designed to ignore outliers. Possibly the oldest of these methods is RANSAC [?], an iterative procedure in which sets of data points are chosen at random and discarded if the agreement between a model fit to them and all other data points falls below a carefully chosen threshold. RANSAC was used for this paper, although other robust methods exist. The criterion developed by [?] deserves special mention in our context; it does away with RANSAC's hard threshold and instead takes into consideration the probability of a match to be in consensus with epipolar geometry.

5.4.2 Using affine oriented FAST, BRIEF and RANSAC to estimate the homography between PIV and ILIDS photographs

Existing PIV/ILIDS systems derive the homography from the result of a camera calibration procedure which the user is required to perform before analyzing images. Although the final value of \mathbf{H} is invisible to the user in our copy of Dantec's DynamicStudio software, the camera matrices \mathbf{P}_{foc} and \mathbf{P}_{def} can be shown and edited. We therefore must find a corrected homography $\hat{\mathbf{H}}$ that allows us to compute

$$\mathbf{P}_{\text{def}} = \hat{\mathbf{H}} \mathbf{P}_{\text{foc}} \quad (5.15)$$

so that we can replace \mathbf{P}_{def} with $\hat{\mathbf{P}}_{\text{def}}$ in the software, effectively correcting \mathbf{H} to $\hat{\mathbf{H}}$.

To efficiently extract keypoints, we combined three algorithms: ASIFT [?] to deal with skew transformations; an oriented version of FAST, published as part of ORB, to detect keypoints; and standard BRIEF as a keypoint extractor.

ASIFT is a method originally developed to be used with SIFT. It introduces invariance to affine mappings by simulating various projective transformations while FAST and BRIEF are run repeatedly. This slows the analysis down, but given the infinitude of possible angled camera-camera-object configurations, it is wise to maintain a flexible framework.

We should note that the original ASIFT with SIFT works well, but SIFT is encumbered by patents. To encourage vendors of imaging systems to adopt the proposed algorithms, we made it our goal to find a freely available replacement.

Recall that the disks in the defocused image are missing from the focused image, rendering a registration between them impossible. It is straightforward to simulate the disks, however. We followed the following protocol on our focused images:

1. Mask the image, blacking out all areas that are known not to contain droplets.
2. Subtract the pixel-wise minimum or mean value taken over all images taken by the camera. This step serves to black out defective hot pixels on the camera's CCD and other static noise.
3. Erode the image, using a 3×3 or 5×5 kernel. This will close any remaining bright pixels which are likely noise.
4. Locate the intensity peaks in the remaining image.
5. Fill a blank image with black, then draw bright circles of diameter D_{disk} onto it, centered at the respective positions of the intensity peaks detected in the focused image. (Note that simply dilating the result of the previous step will not lead to circular disks.)

The result of performing these operations on our sample image is shown in Fig. 5.13. We determined the disk diameter D_{disk} empirically from the defocused images, although it is naturally preferable to automate this step, e.g. using circular Hough transforms or cross-correlation with circular masks. There may be simpler ways of achieving the same result, e.g. by means of Gaussian filters, distance transforms and thresholding operations. However, we found the protocol described above to be quite robust to noise and fast enough for our application.



Figure 5.13: Simulating disks based on the focused image.

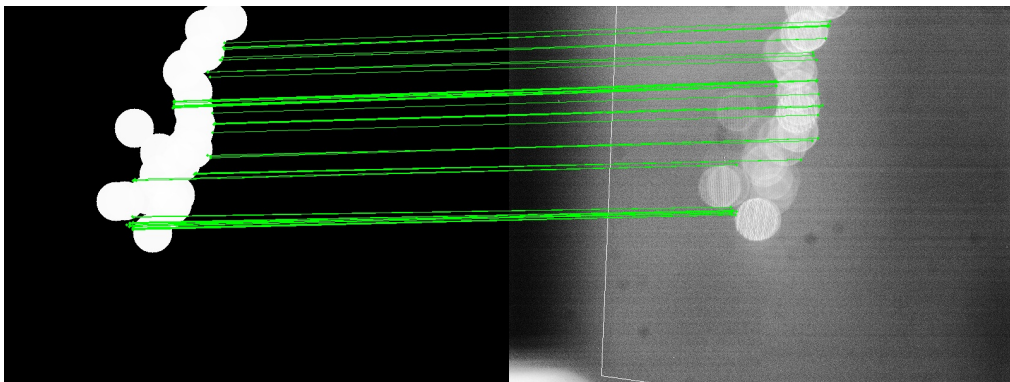


Figure 5.14: Visualized inliers in the set of matched keypoints between the mirrored simulated disks (see Fig. 5.13) and the ILIDS image.

Implementations of ORB and BRIEF are freely available through the OpenCV project, which provides bindings for the C++ and Python languages. We used these implementations to find and extract matching keypoints between our sample images, shown in Fig. 5.14.

The matches shown in Fig. 5.14 were found using a most basic method: brute-force match search, followed by a RANSAC estimation of the homography matrix \mathbf{K} using a threshold of 10.

Since the two cameras were positioned behind a beamsplitter in our setup, the defocused image was flipped horizontally. We therefore first mirrored it horizontally, using

the transformation matrix

$$\mathbf{M}_h = \begin{bmatrix} -1 & 0 & (\text{image width}) \\ 0 & 1 & 0 \\ 0 & 0 & 1 \end{bmatrix}.$$

To speed up the image registration process, it can be helpful to first down-scale the images. To reduce an image to half of its original size, apply

$$\mathbf{S}_{0.5} = \begin{bmatrix} 0.5 & 0 & 0 \\ 0 & 0.5 & 0 \\ 0 & 0 & 1 \end{bmatrix}.$$

While the above operations might not be strictly necessary, we found that they significantly improved the quality of the matches identified. If the registration algorithms mentioned above now find a homography matrix \mathbf{K} , then we can write

$$\mathbf{K} \mathbf{M}_h \mathbf{S}_{0.5} \mathbf{P}_{\text{foc}} = \mathbf{S}_{0.5} \mathbf{P}_{\text{def}} \quad (5.16)$$

and to bring this into a form similar to (5.14),

$$\mathbf{S}_{0.5}^{-1} \mathbf{K} \mathbf{M}_h \mathbf{S}_{0.5} \mathbf{P}_{\text{foc}} = \mathbf{S}_{0.5}^{-1} \mathbf{S}_{0.5} \mathbf{P}_{\text{def}} \quad (5.17)$$

$$= \mathbf{P}_{\text{def}} \quad (5.18)$$

Finally, it turns out that Dantec's DynamicStudio software violates convention by placing the coordinate origin at the bottom (not top) left corner of the image. We must therefore pre- and post-multiply by $\mathbf{M}_v^{\pm 1}$, with

$$\mathbf{M}_v = \begin{bmatrix} 1 & 0 & 0 \\ 0 & -1 & (\text{image height}) \\ 0 & 0 & 1 \end{bmatrix},$$

to arrive at our final expression for $\hat{\mathbf{H}}$:

$$\hat{\mathbf{H}} = \mathbf{M}_v \mathbf{S}_{0.5}^{-1} \mathbf{K} \mathbf{M}_h \mathbf{S}_{0.5} \mathbf{M}_v^{-1}. \quad (5.19)$$

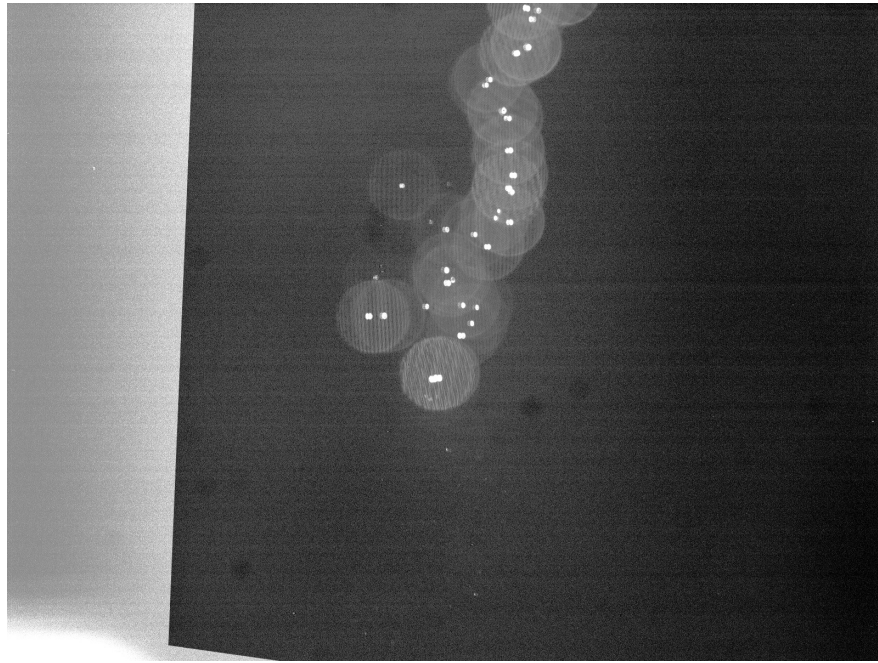


Figure 5.15: Focused camera image, after applying corrected homography $\hat{\mathbf{H}}$ derived from the matched keypoints, is superimposed onto defocused camera image of droplets.

Substitution of $\hat{\mathbf{H}}$ into (5.15) yields $\hat{\mathbf{P}}_{\text{def}}$, which can be manually entered into the DynamicStudio software. Fig. 5.15 illustrates how the use of $\hat{\mathbf{H}}$ leads to an improved alignment compared to Fig. 5.12. Note that a slight projective distortion is necessary for optimal registration, confirming that it is infeasible to restrict the homography to affine matrices.

5.5 Removing center discrepancies with point set registration

The keypoint matching approach described above is not applicable when a slit aperture was used to reduce overlap, as in the paper by Hardalupas *et al.*, so we will outline briefly how to use registration algorithms with such setups.⁵

Keypoints are not required, when the absence of overlap allows us to identify focused

⁵While slit strip images could be simulated over the focused image (in a procedure analogous to that illustrated in Fig. 5.13), the lack of overlap between them could make it significantly more difficult to find “interesting” keypoints in the simulated image.

and defocused objects centers directly from the respective images and find a projection mapping between them. Indeed, Hardalupas *et al.* successfully registered their PIV and ILIDS images that way: using wavelet transforms at various frequencies, they identified the putative droplet centers on both focused and defocused images. Then, using a continuous, single-stream monodisperse droplet generator, they estimated how the magnitude of the center discrepancies varied over the image. After applying this empirically estimated distortion to the captured focused images, they matched each focused droplet to the closest defocused droplet (if one could be found within an subjectively chosen search distance).

Although they reported good success using this method, it requires both an empirical estimation of the center discrepancies every time the camera is defocused *and* a guess at the appropriate search window size. Moreover, mismatches are likely as the naive closest-neighbour search is not robust to noise. To eliminate these steps, we suggest that droplet matches be found directly using a robust point set registration algorithm.

Since the early 1990s, computer vision researchers have accumulated an impressive body of work on this topic, most of it focusing either on rigid transformations (i.e. translation and rotation only) or non-rigid transformations (typically understood to include nonlinear warping). The problem at hand requires an algorithm able to deal with projective transforms, which are non-rigid but linear.

The only paper known to the authors to specifically address this case is by [?], who propose an iterative search based on image moments. Since image moments are an aggregate metric, they do not directly lead to a droplet-to-droplet correspondence. Still, closest-neighbour matches after application of this algorithm would likely produce results no worse than those found after estimating the transformation empirically.

Robust non-rigid methods are also applicable in this case and deserve some mention. Many of them are probabilistic relaxations of the Iterative Closest Point algorithm, which simply searches for the least-squares-optimal rigid mapping. Several of these approaches were reviewed and generalized by [?]. A slightly different approach, named Coherent Point Drift[?], is also highly popular and illustrated in Fig. 5.16.

We forgo at this point a documentation of the application and refer the reader to Hardalupas *et al.*, who describe their center identification technique in good detail, and to the above-mentioned authors, who have published freely available implementations of their algorithms online.

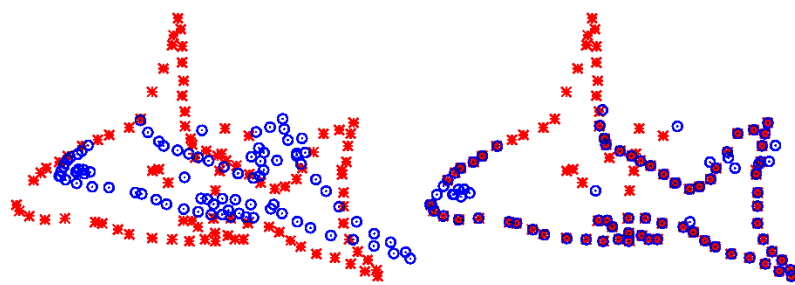


Figure 5.16: Non-rigid variant of the Coherent Point Drift algorithm applied to two point sets. Notice that the probabilistic nature of the matching creates robustness to unmatched points. (Image source: Wikipedia)

Phase-Doppler Particle Analysis (PDPA)

Phase-Doppler anemometry and droplet sizing techniques are based on the far-field intensity fluctuations in the laser light scattered by passing droplets. Unlike ILIDS, however, PDPA uses intersecting laser beams (instead of a laser sheet) to illuminate the droplets. Whereas ILIDS *images* the infringement pattern cast by the glare points on the illuminated droplet, PDPA measures the fringe spacings indirectly by relating them to the phase difference between the signals recorded by a pair of adjacent detectors.

[?] suggested in 1842 that the slight differences in wavelength between the colours of various stars could be used to determine the stars' velocities relative to Earth. A century later, military radar operators during World War II realized that the Doppler effect could be exploited to estimate target velocities using their radar systems. Soon, meteorologists had adopted the technology to measure wind speeds [?]. The flurry of activity around Doppler measurements in the ensuing years produced the first laser-based particle anemometry system, designed in 1964 by [?], and several novel beam-detector configurations have been proposed since. Among them are the popular dual-beam configurations, constituting a departure from the original reference beam systems which can be more difficult to align. A exemplary dual-beam setup is shown in Fig. 6.1.

Laser-Doppler anemometry (LDA, also known as laser-Doppler velocimetry or LDV) provides velocity measurements only. The 1970s saw the discovery that the fringe patterns cast by the scattered light could be analyzed to yield size information [? ?]. This technique is now widely used and often integrated into the detecting and processing hardware of commercial LDA systems, typically under the name of phase-Doppler Anemometry (PDA)

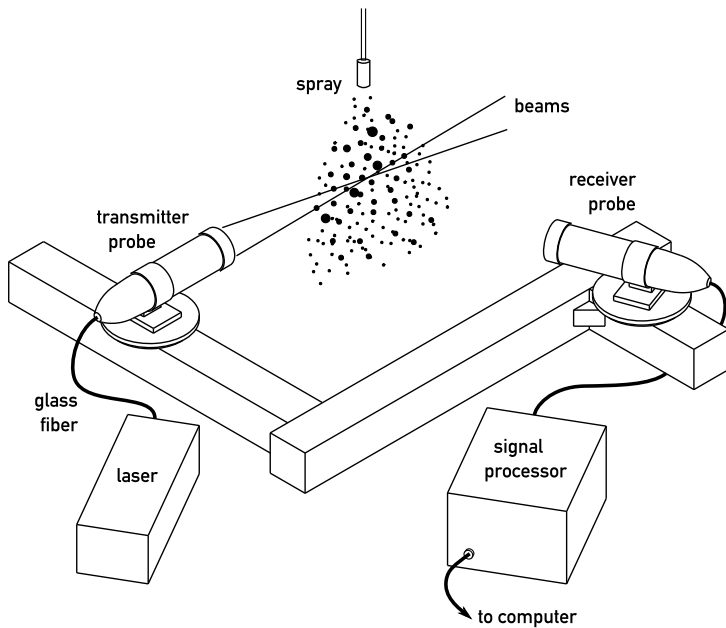


Figure 6.1: Typical commercial PDPA configuration using transmitter and receiver probes

or phase-Doppler particle analysis (PDPA).

PDPA can be used to ascertain droplet size distributions with a very high precision. Nevertheless, its accuracy hinges on the knowledge of a large number of distances, angles and voltages. A single erroneous one of them will throw off the result, leaving the operator none the wiser. We shall therefore discuss briefly the various sources of error in this chapter, and provide some pointers to their resolution. The focus is on measurements of size, not velocity.

6.1 Optical principle

Only droplets passing through the measurement volume have a chance of being detected and characterized, so we will provide here a description of the measurement volume and its interaction with a falling droplet.

To create the measurement volume, two laser beams must intersect where their wave fronts are planar. To this end, the transmitter probe features a front lens which focuses

the beams to a small but finite *waist diameter*. Note that focusing onto an infinitesimally small point is impossible: as the beam is exiting from a finite-sized aperture, some degree of diffraction is unavoidable and will lead to a finite diameter. In the case of most commercial setups, the laser exhibits a Gaussian intensity profile, i.e. the light intensity falls off smoothly with increasing distance from the beam axis. The diffraction of a Gaussian beam generally causes spherically expanding wavefronts [?]; the focusing lens counteracts this effect and leads to plane waves at the beam waist.

Borrowing from the terminology used by [?], the *measurement volume* is the space in which a particle must be located such that it scatters the light onto the detector. For large particles, this will not coincide perfectly with the illuminated volume. The measurement volume contains the *detection volume*, within which a droplet scatters enough light onto the detector to exceed the chosen minimum threshold for detection.

In accord with most introductory texts on PDPA, we will offer two descriptions of the scattering effect experienced by the droplets falling through the measurement volume: a fringe model for very small droplets, and a Moiré model for larger droplets.

6.1.1 Particles smaller than the wavelength

The intersection of the two beams results in their interference at an angle Θ . The alternating extinction and amplification creates a pattern of fringes. As the small droplet (assumed to be a single point) falls through the fringes, it samples the light intensity, scattering an alternating signal onto the detector, which registers a burst of voltage spikes. Since the fringe spacing is known and constant, the detected burst frequency is linearly related to the velocity of the falling droplet.

6.1.2 Large particles

In practice, we do not deal with droplets smaller than tens of microns (much less sub-micron particles, to which the above would apply). We therefore apply a somewhat more complex model, in which the fields of both scattered beams are considered separately. Indeed, their interference is modelled directly at the receiver.

Depending on the relative refractive index m , either the reflected light or the light of a certain scattering order dominates when seen from an off-axis angle φ . In the setup shown in Fig. 6.1, $\varphi = 60^\circ$ and m is assumed to be 1.33 (water droplets in air). In this setup, the receiver will see the beams mostly as first-order refracted rays. An extensive numerical

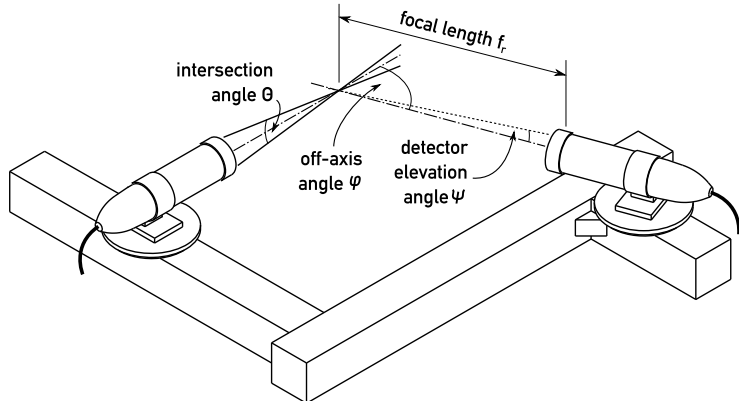


Figure 6.2: Nomenclature used for the geometry in Fig. 6.1

evaluation of these relationships was published by ?].

From the perspective of the receiver, each beam is scattered from a glare point on the droplet surface. Due to the path length differences and the falling motion past the receiver probe, the intensities from both glare points create a beating frequency on both detectors, which are offset in space (on the order of millimeters) and therefore measure the beating signal with slight phase shifts (on the order of a few π). Fig. 6.3 illustrates how larger droplets result in narrower fringes, and thus a larger phase difference.

Note, however, that the patterns shown in Fig. 6.3 are valid only for stationary droplets. Falling droplets experience a Doppler effect: the upward-angled beam is sampled at a relatively higher velocity, leading to a higher scattered frequency. The downward-angled beam, on the other hand, is scattered at a lowered frequency. The discrepancy in frequency leads to curved fringes. Moreover, the direction of the receiver changes as the droplet is falling. The result is not directly intuitive: the velocity has no impact at all on the phase difference between detectors A and B, and the size has no impact on the beat frequency (i.e. burst frequency) measured by the detectors.

For first-order refraction, ?] provide the following relationship between droplet di-

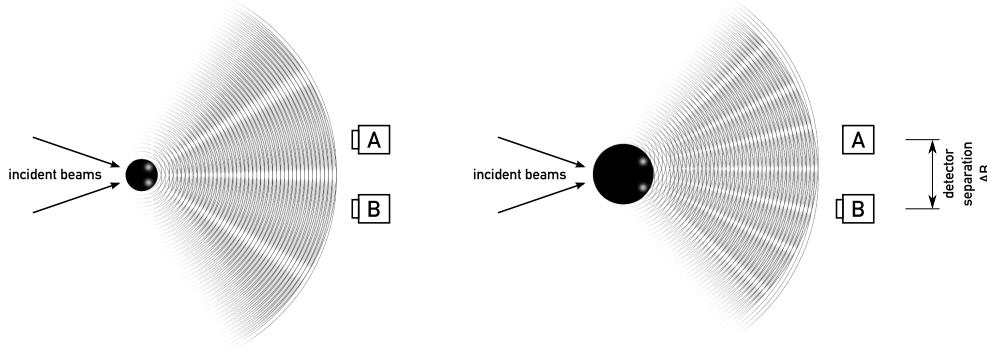


Figure 6.3: Moiré-style visualization of the interference pattern cast by the two glare points. Left: glare points on small particles are close, resulting in wide fringes. The signals recorded by detectors A and B are shifted in time by a phase difference $\Delta\Phi_{AB}$, which is due to the detectors' known separation in space. Right: glare points on larger particles are farther apart, resulting in narrower fringes and a larger phase difference.

diameter d_p and the difference in measured phase Φ between two detectors A and B:

$$\begin{aligned}
 \Delta\Phi_{AB} &= \beta_{AB} d_p \\
 &= \frac{2\pi}{\lambda} (\Phi_A - \Phi_B) d_p \\
 &= \frac{2\pi}{\lambda} d_p \left[\sqrt{1 + m^2 - \sqrt{2}m \sqrt{1 + \sin \psi_A \sin \frac{\Theta}{2} + \cos \psi_A \cos \varphi_A \cos \frac{\Theta}{2}}} \right. \\
 &\quad - \sqrt{1 + m^2 - \sqrt{2}m \sqrt{1 - \sin \psi_A \sin \frac{\Theta}{2} + \cos \psi_A \cos \varphi_A \cos \frac{\Theta}{2}}} \\
 &\quad - \sqrt{1 + m^2 - \sqrt{2}m \sqrt{1 + \sin \psi_B \sin \frac{\Theta}{2} + \cos \psi_B \cos \varphi_B \cos \frac{\Theta}{2}}} \\
 &\quad \left. + \sqrt{1 + m^2 - \sqrt{2}m \sqrt{1 - \sin \psi_B \sin \frac{\Theta}{2} + \cos \psi_B \cos \varphi_B \cos \frac{\Theta}{2}}} \right]. \tag{6.1}
 \end{aligned}$$

Note that Fig. 6.2 explains some of the notation used above.

Because of the periodic nature of the arriving signal, any phase difference value exceeding one period (2π) is indistinguishable from one below one period. One solution to this problem is to consider the signal bursts from both detectors in their entirety and to determine the time shift between them (time shift technique) [?]. Another, more commonly

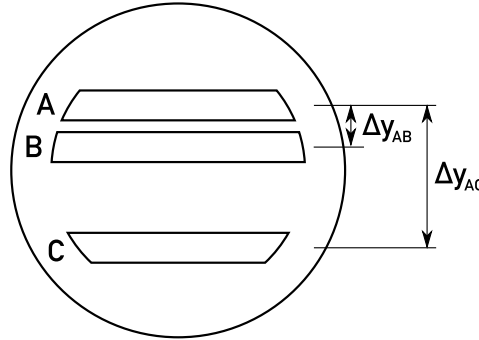


Figure 6.4: Typical vertical arrangement of detectors A, B, and C in a receiver probe. Detector separation values are indicated.

implemented solution is the addition of a third detector, spaced very closely to the first. Then the phase difference between detectors A and C is

$$\Delta\Phi_{AC} = \beta_{AC}d_p. \quad (6.2)$$

Since the slopes β_{AB} and β_{AC} are known, we can then deduce how many 2π jumps should be contained in the measured $\Delta\Phi_{AB}$:

$$n_{2\pi} = \text{int} \left[\frac{1}{2\pi} \left(\frac{\beta_{AB}}{\beta_{AC}} \Delta\Phi_{AC} - \Delta\Phi_{AB} \right) + \frac{1}{2} \right] \quad (6.3)$$

This allows us to bring $\Delta\Phi_{AB}$ into the range $[0, 2\pi]$:

$$\Delta\Phi_{AB} = \beta_{AB}d_p - 2\pi n_{2\pi} \quad (6.4)$$

We are now able to solve for d_p :

$$d_{p,AB} = \frac{\Delta\Phi_{AB} + 2\pi n_{2\pi}}{\beta_{AB}} \quad (6.5)$$

$$d_{p,AC} = \frac{\Delta\Phi_{AC}}{\beta_{AC}} \quad (6.6)$$

If the discrepancy between the two values are below a set threshold, the measurement is accepted.

Generally, the elevation angle ψ of a given detector is not known. However, it can

be estimated from the detector separation values (see Fig. 6.4) and the focal length of the receiver's lens f_r .

6.1.3 Calculation in TSI FlowSizer software

To verify the results displayed by the TSI FlowSizer software, it was necessary to understand how FlowSizer arrives at a diameter distribution from the measured phase data. Although their algorithm is not published, it is possible to reverse engineer their approach by deriving the required mathematical simplifications. We then compared the results to an implementation of the full equation given above, based on a set of raw detector phase data.

FlowSizer records the phase differences between detector pairs AB and AC, ranging from -180° to 180° . We must first adjust these values to yield strictly positive phase differences. To this end, we add 360° to all negative phase difference values to map them onto equivalent phpositive phase differences.

[] then provide a simple approximation of (6.1) under a number of assumptions (e.g. $\sin \psi \approx \psi$ etc.):

$$\Delta\Phi_{AB} \approx -\frac{2\pi}{\lambda} d_p \sin \psi_{AB} \sin \frac{\Theta}{2} \frac{m}{v\sqrt{1+m^2-mv}} \quad (6.7)$$

$$\Delta\Phi_{AC} \approx -\frac{2\pi}{\lambda} d_p \sin \psi_{AC} \sin \frac{\Theta}{2} \frac{m}{v\sqrt{1+m^2-mv}}, \quad (6.8)$$

with

$$v_{AB} = \sqrt{2(1 + \cos \psi_{AB} \cos \varphi \cos \frac{\Theta}{2})} \quad (6.9)$$

$$v_{AC} = \sqrt{2(1 + \cos \psi_{AC} \cos \varphi \cos \frac{\Theta}{2})} \quad (6.10)$$

FlowSizer first makes the assumption that $\cos \psi_{AB} \approx \cos \psi_{AC} \approx 0.995$, and thus simply computes

$$v = \sqrt{2(1 + 0.995 \cos \varphi \cos \frac{\Theta}{2})} \quad (6.11)$$

They also designate as “slope” (here, γ) the second term of (6.7) and (6.8):

$$\gamma = \frac{m}{v\sqrt{1+m^2-mv}}. \quad (6.12)$$

Also, the fringe distance at the center of the illuminated volume, given perfect alignment, is given by [] to be:

$$\delta x = \frac{\lambda}{2 \sin \frac{\Theta}{2}}. \quad (6.13)$$

Finally, FlowSizer appears to use the approximation

$$\sin \psi_{AB} = \frac{\Delta y_{AB}/2}{f_r} \quad (6.14)$$

$$\sin \psi_{AC} = \frac{\Delta y_{AC}/2}{f_r}, \quad (6.15)$$

where Δy_{AB} is the physical separation between detectors A and B (e.g. in millimeters) and f_r is the focal length of the receiver lens.

It follows that (6.7) and (6.8), when rewritten for β , can be composed as

$$\beta_{AB} = \frac{\Delta y_{AB}}{2f_r} \gamma \frac{360^\circ}{\delta x} \quad (6.16)$$

$$\beta_{AC} = \frac{\Delta y_{AC}}{2f_r} \gamma \frac{360^\circ}{\delta x} \quad (6.17)$$

Where we write 360° instead of 2π since FlowSizer works with phase values in degrees. This is a useful approximation, because now β_{AB} and β_{AC} only depend on constant values (including Δy_{AB} and Δy_{AC} , which can be set in the software).

FlowSizer then filters out all $d_{p,AB}, d_{p,AC}$ pairs that differ by more than some threshold. The manual recommends seven percent of the maximum measureable size, which in practice evaluates to a few tens of microns.

6.1.4 Calibration in TSI FlowSizer

It follows from the above equations that no calibration should be necessary at all, as long as all angles and distances are well-known. However, Δy_{AB} and Δy_{AC} are not typically known to great precision. The solution, then, is to determine their values based on the phase differences recorded after measuring monodisperse droplets of known size.

The TSI FlowSizer software provides this functionality. Presuming a vibrating orifice droplet generator is used, flow rate and frequency can be entered and are converted to droplet diameter using (4.1). The software then adjusts Δy_{AB} and Δy_{AC} such that the peak (if any) or some still-unknown measure of average of the diameter distribution aligns with the expected droplet diameter. This is easily done, since due to the approximation of $\cos \psi \approx 0.995$, the value of γ no longer depends on Δy_{AB} and Δy_{AC} and can be set independently.

6.2 Sources of error

6.2.1 Gaussian beam divergence

The theory predicting the linear relationship between detector phase difference and droplet diameter is founded on the assumption of very small droplets and plane beam wavefronts. Unfortunately, when particles larger than the beam cross the measurement volume in certain directions, glare points of the normally dominant scattering order (e.g. first-order refraction) can temporarily become weak enough to be dominated by another scattering order (e.g. reflection). This phenomenon leads to erroneous results, of course, and is termed *trajectory ambiguity effect* (TAE) or *Gaussian beam defect* (GBD) in the literature.

The problem was recognized first by [?], but had to be neglected until the plane-wave scattering theory of Lorenz-Mie optics was extended into the *Generalized Lorenz-Mie Theory* (GLMT). Most of this work was done by Gouesbet, Gréhan, Maheu, Lock and others throughout the 1980s [? ? ? ?], and mathematically rigorous formulations were available by the early 1990s [? ?]. The 1996 paper by Gouesbet and Gréhan summarizes these developments and provides an early overview over the attempts to circumvent the TAE [?].

Solutions proposed in [?] include planar setups (a different geometry, in which detectors are placed in line with the beams) and validity checks between the diameter determined by detector pairs AB and AC.

6.2.2 Slit effect

Most commercial phase-Doppler systems use a slit aperture in front of the detector or receiving fibers [?]. This helps to define the detection volume in the z dimension (i.e. the beam direction), which is necessary for further statistics about flux, and it can be useful

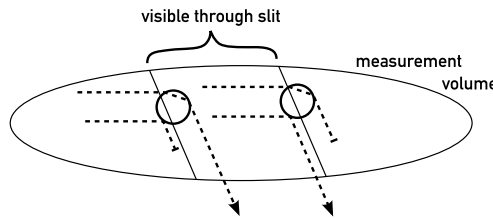


Figure 6.5: Schematic illustrating the slit effect. Two small droplets are passing through the measurement volume (top view; trajectories are into the page). The droplet on the left only scatters its refracted glare point onto the receiver (as normally intended at $\varphi = 60^\circ$). Refraction is suppressed, however, for the droplet on the right; the slit aperture only allows the reflected light to pass.

when sprays are very dense, as multiple droplets may be present within the measurement volume at a time.

It can occur, however, that the aperture cuts off the dominant-order glare point of a droplet that is just halfway outside of the visible region. In that case, the glare point corresponding to the non-dominant scattering order will dominate and result in a wrong measurement. A graphical representation is shown in Fig. 6.5.

Durst et al show experimentally that the slit effect is even more crucial than the Gaussian beam effect. [?]. Together with the TAE, this is called the measurement volume effect. As with the slit effect, three-detector setups are significantly less sensitive to this problem because of the additional validation. Qiu and Hsu propose using four detectors, instead of three, to resolve this problem entirely [?]. A similar design was verified experimentally by [?].

A more recent review of the phenomenon and associated techniques was published by [?].

6.2.3 Change in fringe frequency over z

The sphericity of the beam wavefronts causes the fringe spacing to vary along the major axis of the measurement volume. At the near and far ends of the volume, the fringes are spaced farther apart, which can result in an error on the order of 10% according to [?]. The most important factor is the beam waist dislocation (i.e. misalignment), which must be minimized. The error is also reduced for wider beam waists and larger intersection angles Θ .

6.2.4 Selection of lenses and masks

?] have shown that the selection of lenses and detector masks can have a considerable effect on droplet sizing results. In their experiment, they measured the same spray using several combinations of focal lengths and mask sizes and found that if the diameter range to be measured is not known *a priori*, it can be very difficult to choose an appropriate lens-mask combination.

6.2.5 Optical aberrations

?] investigated several error sources arising in PDPA calibration, and found that the spherical aberration of the transmitter lens typically gave errors of less than 3%.

6.2.6 Dirty fiber ends

The ends of the transmitter fibers should be polished regularly. Dirty or scratched fiber ends can mar the Gaussian beam profiles, leading to distortions or irregularities in the measurement volume's fringe pattern.

6.2.7 Wrongly entered parameters

The optical principle involves many more geometric parameters than are needed for the operation of ILIDS or laser diffraction (Malvern) devices. As a result, an excellent interface and a very attentive user are required to ensure accurate results.

In practice, I always get error messages when doing the last step, and the values are way out of the expected range. The result, then, is that the D20 is made very close to the expected monodisperse diameter. Since the D20 is quite a bit larger than the actual (and completely obvious) peak value, even these "wrong" values aren't correct.

6.3 Calibration

If all optical parameters are known, the equations necessary to derive droplet diameters and velocities are fully determined. However, Δy_{AB} and Δy_{AC} are not always known to high accuracy and can, in fact, undergo slight changes if the receiver is subject to mechanical vibrations over the years. The FlowSizer software therefore offers a calibration tool to help

determine empirical values for Δy_{AB} and Δy_{AC} given a set of measurements of droplets of known size.

To calibrate, we must solve for the two values under the requirement that the peak of the diameter histogram coincide with the known droplet diameter. This is not straightforward for a few reasons:

- The epsilon cutoff criterion means that obtaining the diameter histogram from the phase differences is a one-way calculation (a cutoff cannot be reversed algebraically)
- The choice of "peak" diameter is questionable. If the measured diameter distribution is not exactly symmetrical, it may be preferable to use a form of average (e.g. D_{10}, D_{20}, D_{32}) instead of the diameter corresponding to the true maximum. Alternatively, a Gaussian kernel density estimate of some arbitrary bandwidth may be used.
- Since there is no unique pair of values for Δy_{AB} and Δy_{AC} that will result in the expected peak diameter, an additional relationship must be used to establish the best pair. One source for this could be the difference-diameter plot: one could minimize the sum of absolute or squared differences between AB and AC measurements.

The combination of the above three points means that an iterative search for the optimal $\Delta y_{AB}/\Delta y_{AC}$ combination is inevitable. Alternatively, we can find the set of possible combinations given one set of measurements, then find overlaps with the sets of possible combinations from other measurement sets. This has been very difficult to do in our experience, as shown in Fig. 6.6.

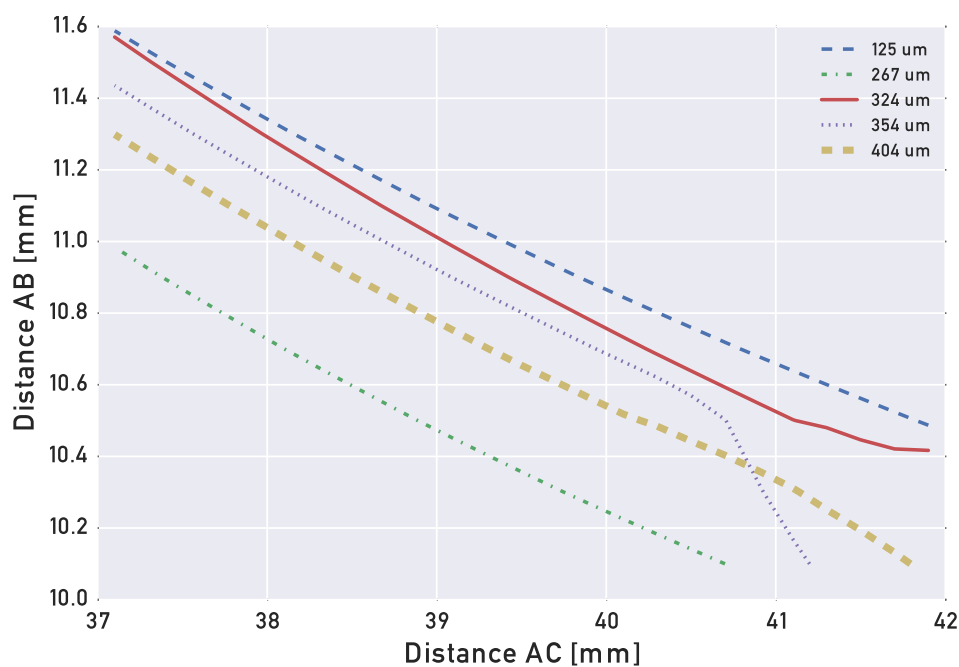


Figure 6.6: Result of a set of calibration attempts showing the difficulty in finding a consistent pair of Δy_{AB} and Δy_{AC} values. Each line corresponds to a set of potential values for Δy_{AB} and Δy_{AC} that would yield a diameter distribution with a peak at the known diameter value shown in the legend.

Breakup of a liquid jet when colliding with a gas jet

Impinging-jet injectors are often used in liquid-propellant rockets.

A relevant experimental study was recently performed by [?] in the context of Kraft smelt shattering in the paper industry. To convert wood chips into pulp fit for paper production, they are boiled in a strongly alkaline solution of sodium salts (lye and sodium sulfate). Over time, wood residue accumulates in the liquid. To recover the sodium salts, the organic material is burned off in a so-called *Kraft recovery boiler*. The molten salts collect at the bottom of the furnace as *smelt*. The smelt can be quenched in water, but must be atomized (“shattered”) before making contact with the water to prevent too sudden a release of steam which can damage the boiler. The interaction of smelt and water has been studied in detail, most recently by [?].

While fundamental studies on impinging liquid-liquid jets abound, publications on liquid-gas impingement are sparse. An impressive amount of experimental data on “gas-augmented injectors” was produced by Rocketdyne for NASA in 1970 [?]. Rakesh, in recent papers [? ?], has made claims about the relationship between mass flow ratios, gas pressure and drop size distribution for impinging liquid-gas doublets. None of these works include any photographic documentation or high-level discussion of the breakup process, however. This paper is our attempt to fill that gap.

(We also mention the relationship to jet-in-crossflow experiments, liquid sheet shear breakup experiments and simulations, and air jet dimple making experiments.)

Our experimental setup shares many characteristics with that of jet-in-crossflow experiments (where the crossflow is significantly larger than the jet) and with water-water

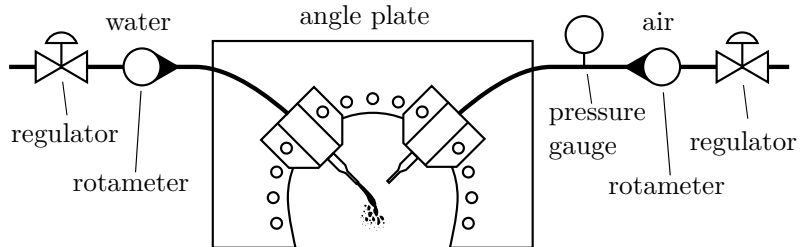


Figure 7.1: Our test rig. Cameras can be positioned on tripods to capture the breakup from different angles.

impingement studies.

Several jet-jet impingement studies have been published since ?], e.g. the recent analysis by ?].

7.1 Experimental setup

Our setup, shown schematically in Fig. 7.1, consists of a plate about 15 cm in length, upon which two small assemblies holding Luer fittings can be mounted at various angles. The Luer fittings accommodate blunt hypodermic needles of arbitrary diameter; the needles in turn are fed with water and air at carefully regulated flow rates. Both fluids are at room temperature.

A detail of the angle plate is given in Fig. 7.2.

1. Types of runs/configurations
2. Results (photos, videos)

7.2 Discussion

7.2.1 Description of regimes observed

Comparison with other papers/authors

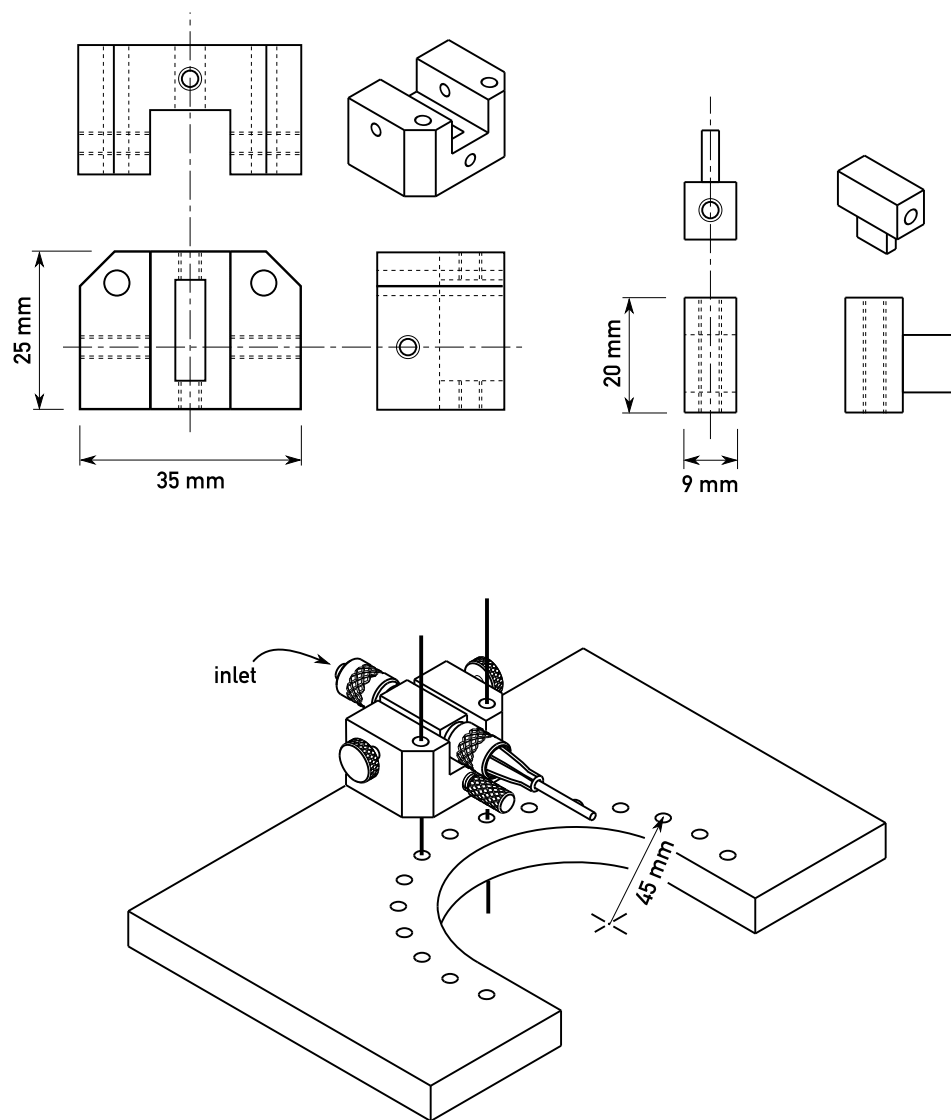


Figure 7.2: Angle plate setup. Only one needle holder assembly is shown; two are necessary to perform the experiment.

7.2.2 Correlation of regimes with other numbers/factors

Blabla

7.2.3 Interesting bits and pieces

Waviness/shear effect

Since the air is so much faster than the water, it takes the water with it. This strongly amplifies the impact waves we see.

This was predicted by ?] and ?].

Using a gas for impingement has two consequences: first, the gas must travel significantly faster than the liquid to carry the same momentum:

$$\dot{m}_l v_l = \dot{m}_g v_g \quad (7.1)$$

$$(\rho_l A_l v_l) v_l = (\rho_g A_g v_g) v_g \quad (7.2)$$

$$\frac{v_g}{v_l} = \sqrt{\frac{\rho_l A_l}{\rho_g A_g}}. \quad (7.3)$$

As a result, the gas acts as a shearing force on the crests of impact waves on the sheet. This results in small sheets tearing off (Fig. ??). Their rims can be clearly seen in photographs (Fig. ??).

There are digitations along the edges.

Holes in a moving sheet

As a transition region ...

Bell on top

This happens when the small water is very thin and the big water closes around it.

Sheet behind

This happens when the water is thin but doesn't cause a bell.

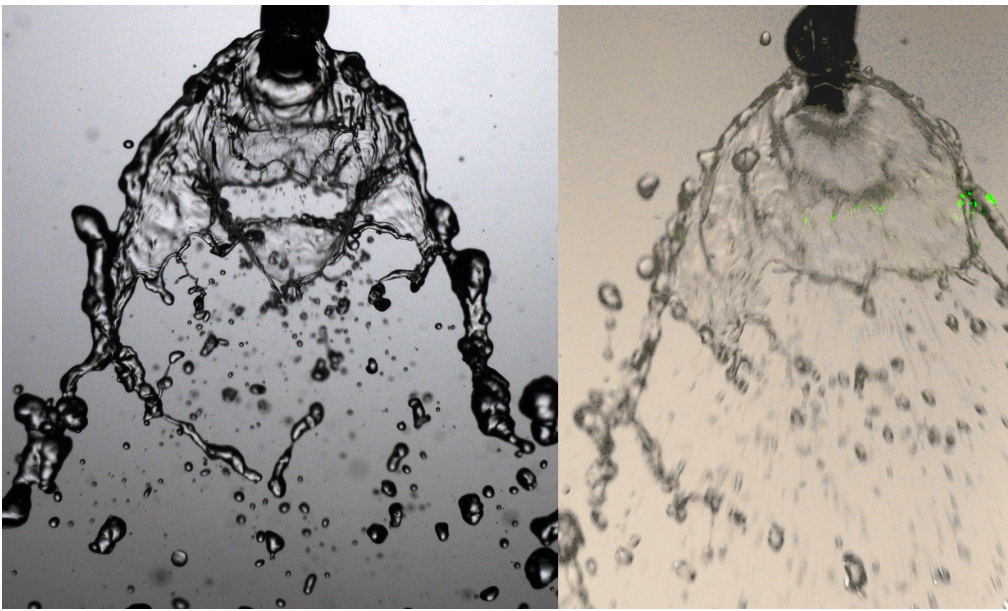


Figure 7.3: shear effect along the sheet

7.3 Geometric analysis

The shape of the sheet is mainly due to the balance between inertial forces driving it apart and curvature energy (i.e. surface tension) drawing it together. By equating these two forces in the cylindrical coordinate system shown in Fig. ??, we can arrive at an expression for the shape $y(x)$ of a single streamline at an angle φ :

$$2\sigma \left(\frac{1}{R_c} + \frac{\cos(\tan^{-1} y')}{y} \right) = \frac{\nu^2 \rho t(x, \varphi)}{R_c}, \quad (7.4)$$

where R_c is the radius of curvature in the x - y plane, defined as

$$R_c = \frac{\left(\sqrt{1+y'^2} \right)^3}{|y''|}. \quad (7.5)$$

The second term in the bracket corresponds to the curvature in the y - ϑ plane, while the right-hand side represents the resulting centripetal effect on the sheet.

Note that unlike Lance and Perry, we are ignoring both gravity and pressure differ-

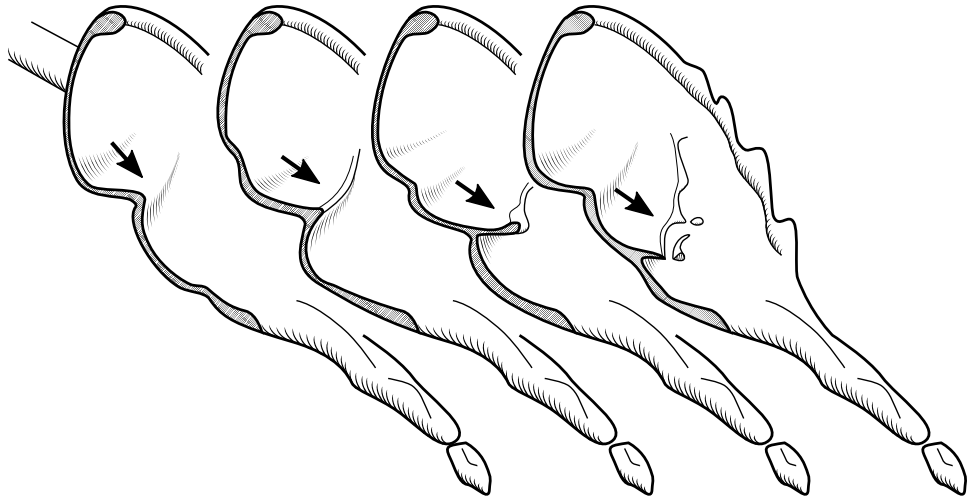


Figure 7.4: Conceptualization of the shear effect along the sheet

entials acting on the sheet in the normal direction. This simplifies our analysis, but does not reduce explanatory power significantly as long as we are dealing with liquid-liquid impingement at high velocities.

Let us model the thickness of the sheet at an angle φ as follows. Naber and Reitz put forward an empirical approximation of the thickness of a flat sheet:

$$t_0(\varphi) = \frac{\beta r_j \sin \vartheta}{2(e^\beta - 1)} e^{\beta \varphi / \pi}, \quad (7.6)$$

where β can be found from

$$\cos \vartheta = \left(\frac{e^x + 1}{e^x - 1} \right) \frac{1}{1 + (\pi/\beta)^2}. \quad (7.7)$$

For a flat sheet, this thickness is valid at a circle of radius $r_0 = \frac{r_j}{\sin \vartheta}$. If we assume that thickness decreases radially, then we should divide the above expression by y/r_0 , which, after cancelling terms, becomes

$$t(x, \varphi) = \frac{\beta r_j^2 e^{\beta \varphi / \pi}}{2y(e^\beta - 1)}. \quad (7.8)$$

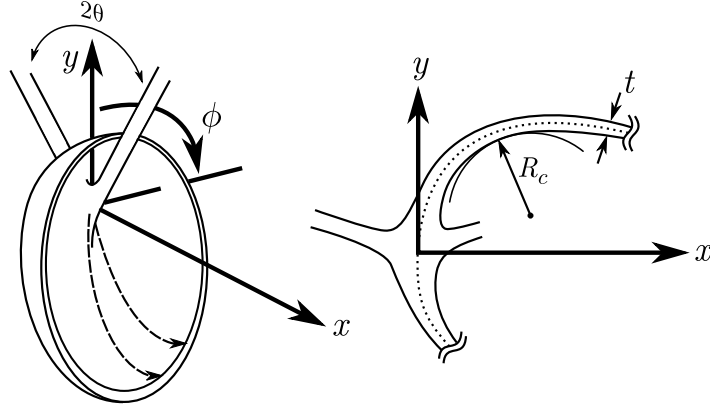


Figure 7.5: Cylindrical coordinate system used in our analysis. We rely on the assumption that every streamline (dashed) follows a single angle φ and can therefore be described by the distance y from a horizontal axis x .

After substituting this into (??), cancelling terms and using the identity

$$\cos(\tan^{-1} y') = \frac{1}{\sqrt{1+y'^2}}, \quad (7.9)$$

we get

$$y'' = \pm \frac{(1+y'^2)}{\frac{v^2 \rho \beta r_j^2 e^{\beta \varphi / \pi}}{4\sigma(e^\beta - 1)} - y}. \quad (7.10)$$

Laplace transforms lead to the unique solution

$$y(x) = \frac{v^2 \rho T(\varphi)}{2\sigma} - \sqrt{C_1 - x^2 - 2C_2 x - C_2^2}, \quad (7.11)$$

where

$$C_1(\varphi) = (y'_0)^2 + 1 \left(\frac{v^2 \rho T(\varphi)}{2\sigma} - y_0 \right)^2, \text{ and} \quad (7.12)$$

$$C_2(\varphi) = y'_0 \left(\frac{v^2 \rho T(\varphi)}{2\sigma} - y_0 \right). \quad (7.13)$$

Here, $y_0 = y(r_0)$ and $y'_0 = y'(r_0)$. Note the similarity to the shape of a true circle, $y(x) = \sqrt{1-x^2}$.

Bibliography

- H.-E. Albrecht, M. Borys, N. Damaschke, and C. Tropea. *Laser Doppler and Phase Doppler Measurement Techniques*. Springer, 2003.
- E. Hecht. *Optics*. Addison-Wesley Longman, Incorporated, 2002. ISBN 9780805385663. URL <http://books.google.ca/books?id=7aG6QgAACAAJ>.
- H. van de Hulst. *Light Scattering by Small Particles*. Dover Books on Physics. Dover Publications, 2012.
- L. N. Ng. *Manipulation of Particles On Optical Waveguides*. PhD thesis, University of Southampton, September 2000.
- W. H. Walton and W. C. Prewett. The production of sprays and mists of uniform drop size by means of spinning disc type sprayers. *Proceedings of the Physical Society B*, 62: 341–350, Jun 1949.
- C. R. Merritt and J. A. Drinkwater. A laboratory device for producing single drops in uniform sizes of 150–450 μm diameter. *Pesticide Science*, 8:457–562, 1977.
- C. R. Allan, H. R. Carlon, A. K. Stuempfle, T. E. Hoffer, and R. L. Pittier. Survey of the literature: Controlled generation of liquid droplets. Technical Report TR-88164, Chemical Research, Development & Engineering Center, U.S. Army Munitions Chemical Command, Aug 1988.
- W. R. Lane. A microburette for producing small liquid drops of known size. *Journal of Scientific Instruments*, 24:98, Apr 1947.
- K. Reil and J. Hallett. An apparatus for the production of uniform sized water drops, at desired time intervals. *Review of Scientific Instruments*, 40:533–534, Apr 1969.

- S. Coggins and E. A. Baker. Micro sprayers for the laboratory application of pesticides. *Annals of Applied Biology*, 102:149–154, Feb 1983.
- W. J. Stry. *The combustion of free flowing droplets of chlorinated benzenes, alkanes, and their mixtures*. PhD thesis, SUNY Buffalo, September 1992.
- I. Endo, Y. Sato, S. Saito, T. Nakagiri, and S. Ohno. Bubble jet recording method and apparatus in which a heating element generates bubbles in a liquid flow path to project droplets, February 2 1988. US Patent 4,723,129.
- A. V. Sergeyev and R. A. Shaw. An inexpensive uniform-size aerosol generator. *Measurement Science and Technology*, 17:N41, 2006.
- J. C. Yang, W. Chien, M. King, and W. L. Grosshandler. A simple piezoelectric droplet generator. *Experiments in Fluids*, 23:445–447, 1997.
- H. Ulmke, T. Wriedt, and K. Bauckhage. Piezoelektrischer Tropfengenerator zur Kalibrierung von Partikelzählern. *Chemie Ingenieur Technik*, 71(12):1387–1391, 1999.
- H. P. Le. *Progress and trends in inkjet printing technology*, volume 42.
- E. Lee. *Microdrop Generation*. Nano- and Microscience, Engineering, Technology and Medicine. Taylor & Francis, 2002.
- A. Amirzadeh Goghari and S. Chandra. Producing droplets smaller than the nozzle diameter by using a pneumatic drop-on-demand droplet generator. *Experiments in Fluids*, 44:105–114, Jan 2008.
- G. J. Green, D. E. Walsh, F. Takahashi, and F. L. Dryer. Aerodynamic device for generating mono-disperse fuel droplets. *Review of Scientific Instruments (ISSN 0034-6748)*, 60:646–652, Apr 1989.
- F. Savart. Memoire sur la constitution des veines liquides lancees par des orifices circulaires en mince paroi. *Annales de Chimie et de Physique*, 53:337–386, 1833.
- L. Rayleigh. On the capillary phenomena of jets. *Proceedings of the Royal Society of London*, 29:71–97, 1879.
- R. J. Donnelly and W. Glaberson. Experiments on the capillary instability of a liquid jet. *Proceedings of the Royal Society of London. Series A. Mathematical and Physical Sciences*, 290(1423):547–556, 1966. doi: 10.1098/rspa.1966.0069.

- J. M. Schneider and C. D. Hendricks. Source of uniform-sized liquid droplets. *Review of Scientific Instruments*, 35:1349–1350, Oct 1964.
- R. N. Berglund and B. Y. H. Liu. Generation of monodisperse aerosol standards. *Environmental Science and Technology*, 7:147–153, Feb 1973.
- J. L. Dressler and G. O. Kraemer. A multiple drop-size drop generator for calibration of a phase-doppler particle analyzer. *Liquid Particle Size Measurement Techniques*, 2 (1083):30–44, 1990.
- L. Ström. The generation of monodisperse aerosols by means of a disintegrated jet of liquid. *Review of Scientific Instruments*, 40:778–782, Jun 1969.
- G. König, K. Anders, and A. Frohn. A new light-scattering technique to measure the diameter of periodically generated moving droplets. *Journal of Aerosol Science*, 17: 157–167, 1986.
- A. R. Glover, S. M. Skippon, and R. D. Boyle. Interferometric laser imaging for droplet sizing: a method for droplet-size measurement in sparse spray systems. *Applied Optics*, 34:8409–8421, Dec 1995.
- G. Pan, J. Shakal, W. Lai, R. Calabria, P. Massoli, and O. Pust. Simultaneous global size and velocity measurement of droplets and sprays. *Spray '06 – Workshop über Sprays, Erfassung von Sprühvorgängen und Techniken der Fluidzerstäubung*, 2006.
- T. Kawaguchi, Y. Akasaka, and M. Maeda. Size measurements of droplets and bubbles by advanced interferometric laser imaging technique. *Meas Sci Technol*, 13:308–316, Feb 2002.
- C. Mounaïm-Rousselle and O. Pajot. Droplet sizing by mie scattering interferometry in a spark ignition engine. *Part Part Syst Charact*, 16:160–168, 1999.
- N. Damaschke, H. Nobach, and C. Tropea. Optical limits of particle concentration for multi-dimensional particle sizing techniques in fluid mechanics. *Experiments in Fluids*, 32:143–152, 2002.
- M. Maeda, Y. Akasaka, and T. Kawaguchi. Improvements of the interferometric technique for simultaneous measurement of droplet size and velocity vector field and its application to a transient spray. *Experiments in Fluids*, 33:125–134, Jun 2002.

- N. Damaschke, S. Rasmussen, C. Tropea, and A. Woite. Global phase doppler technique. In *6th International Congress on Optical Particle Characterisation, Brighton, UK*, 2001.
- A. Quérel, P. Lemaitre, M. Brunel, E. Porcheron, and G. Gréhan. Real-time processing algorithm of global interferometric laser imaging for the droplet sizing (ilids) in airborne research. In *15th International Symposium on Applications of Laser Techniques to Fluid Mechanics*, Jul 2010.
- Y. Hardalupas, S. Sahu, A. M. K. P. Taylor, and K. Zarogoulidis. Simultaneous planar measurement of droplet velocity and size with gas phase velocities in a spray by combined ilids and piv techniques. *Experiments in Fluids*, 49:417–434, 2010.
- Y. Hardalupas, S. Sahu, and A. M. K. P. Taylor. Measurement of vapour concentration and droplet size and velocity in an evaporative spray. In *15th International Symposium on Applications of Laser Techniques to Fluid Mechanics*, Jul 2010.
- R. Kurosawa, K. Hishida, and M. Maeda. Combined measurement of lif and ilids for vapor concentration and droplets size and velocity in a spray. In *11th International Symposium on Applications of Laser Techniques to Fluid Mechanics, Lisbon, Portugal*, 2002.
- C. Harris and M. Stephens. A combined corner and edge detector. In *Proceedings of the Alvey Vision Conference 1988*, pages 23.1–23.6, Jan 1988.
- D. G. Lowe. Distinctive image features from scale-invariant keypoints. In *International Journal of Computer Vision*, volume 60, page 91, Nov 2004.
- H. Bay, A. Ess, T. Tuytelaars, and L. V. Gool. Speeded-up robust features (surf). *Computer Vision and Image Understanding*, 110:346–359, 2008.
- S. Leutenegger, M. Chli, and R. Y. Siegwart. Brisk: Binary robust invariant scalable keypoints. In *2011 IEEE International Conference on Computer Vision (ICCV)*, pages 2548–2555, 2011.
- M. Agrawal, K. Konolige, and M. R. Blas. Censure: Center surround extremas for realtime feature detection and matching. In *10th European Conference on Computer Vision*, pages 102–115, 2008.

- E. Rosten and T. Drummond. Fusing points and lines for high performance tracking. In *2005 IEEE International Conference on Computer Vision (ICCV)*, volume 2, pages 1508–1515, 2005.
- E. Rublee, V. Rabaud, K. Konolige, and G. Bradski. Orb: an efficient alternative to sift or surf. In *2011 IEEE International Conference on Computer Vision (ICCV)*, pages 2564–2571, Nov 2011.
- M. Calonder, V. Lepetit, C. Strecha, and P. Fua. Brief: Binary robust independent elementary features. In *11th European Conference on Computer Vision*, volume LNCS 6314, pages 778–792, 2010.
- M. Muja and D. G. Lowe. Fast approximate nearest neighbours with automatic algorithm configuration. In *International Conference on Computer Vision Theory and Applications*, pages 331–340, Feb 2009.
- M. A. Fischler and R. C. Bolles. Random sample consensus: A paradigm for model fitting with applications to image analysis and automated cartography. *Communications of the ACM*, 24:381–395, Jun 1981.
- L. Moisan and B. Stival. A probabilistic criterion to detect rigid point matches between two images and estimate the fundamental matrix. *International Journal of Computer Vision*, 57:201–218, 2004.
- J.-M. Morel and G. Yu. Asift: a new framework for fully affine invariant image comparison. *SIAM Journal on Imaging Sciences*, 2:438–469, 2009.
- Y.-T. Chi, J. Ho, and M.-H. Yang. A direct method for estimating planar projective transform. In *10th Asian Conference on Computer Vision*, pages 268–281, 2011.
- B. Jian and B. C. Vemuri. Robust point set registration using gaussian mixture models. *IEEE transactions on pattern analysis and machine intelligence*, Dec 2010.
- A. Myronenko and X. Song. Point set registration: coherent point drift. *IEEE transactions on pattern analysis and machine intelligence*, 32:2262–2275, Dec 2010.
- C. Doppler. Über das farbige licht der doppelsterne und einiger anderer gestirne des himmels. *Abhandlungen der k. böhm. Gesellschaft der Wissenschaften*, 5:465–482, 1842.

- R. C. Whiton, P. L. Smith, S. G. Bigler, K. E. Wilk, and A. C. Harbuck. History of operational use of weather radar by u.s. weather services. part ii: Development of operational doppler weather radars. *Weather and Forecasting*, 13:244–252, 1998.
- Y. Yeh and H. Z. Cummins. Localized fluid flow measurements with an he-ne laser spectrometer. *Applied Physics Letters*, 4:176–178, May 1964.
- F. Durst and M. Zare. Laser Doppler measurements in two-phase flows. In P. Buchhave, J. M. Delhaye, F. Durst, W. K. George, K. Refslund, and J. H. Whitelaw, editors, *The Accuracy of Flow Measurements by Laser Doppler Methods, Proceedings of the LDA-Symposium '95, Copenhagen, Denmark*, pages 403–429, 1976.
- G. Wigley. The sizing of large droplets by laser anemometry. *Journal of Physics E: Scientific Instruments*, 11:639–642, 1978.
- K. Thyagarajan and A. Ghatak. *Lasers: Fundamentals and Applications*. Graduate Texts in Physics. Springer, 2010.
- A. Naqwi and R. Menon. A rigorous procedure for design and response determination of phase doppler systems. In *Proceedings of the 7th International Symposium on Applications of Laser Anemometry to Fluid Mechanics, Lisbon, Portugal*, pages 340–353, 1994.
- M. Saffman. The use of polarized light for optical particle sizing. In *Proceedings of the 3rd International Symposium on Applications of Laser Anemometry to Fluid Mechanics, Lisbon, Portugal*, page 18.2, 1986.
- G. Gréhan, G. Gouesbet, and C. Rabasse. The computer program supermidi for lorenz-mie theory and the research of one-to-one relationships for particle sizing. In *Proceedings of the symposium on long range and short range optical velocity measurements*, Institut franco-allemand de Saint-Louis, September 1980.
- G. Gouesbet and G. Gréhan. Sur la généralisation de la théorie de lorenz-mie. *Journal of Optics*, 13(2):97–103, 1982.
- G. Gouesbet, B. Maheu, and G. Gréhan. Light scattering from a sphere arbitrarily located in a gaussian beam, using a bromwich formulation. *Journal of the Optical Society of America A*, 5(9):1427–1443, 1988.

- B. Maheu, G. Gouesbet, and G. Gréhan. A concise presentation of the generalized lorenz-mie theory for arbitrary location of the scatterer in an arbitrary incident profile. *Journal of Optics*, 19(2):59–67, 1988.
- J. A. Lock and G. Gouesbet. A rigorous justification of the localized approximation to the beam shape coefficients in generalized lorenz-mie theory, i. on-axis beams. *Journal of the Optical Society of America A*, 11(9):2503–2515, 1994.
- G. Gouesbet and J. A. Lock. A rigorous justification of the localized approximation to the beam shape coefficients in generalized lorenz-mie theory, ii. off-axis beams. *Journal of the Optical Society of America A*, 11(9):2516–2525, 1994.
- G. Gouesbet and G. Gréhan. Gaussian beam errors in phase-doppler anemometry and their elimination. In R. Adrian, D. Durão, F. Durst, M. Heitor, M. Maeda, and J. Whitelaw, editors, *Developments in Laser Techniques and Applications to Fluid Mechanics*, pages 243–259. Springer Berlin Heidelberg, 1996.
- F. Durst, C. Tropea, and T.-H. Xu. The slit effect in phase doppler anemometry. In *Modern techniques and measurements in fluid flows: Proceedings of the 2nd International Conference on Fluid Dynamic Measurement and Its Applications*, Oct 1994.
- H. Qiu and C. T. Hsu. Method of phase-doppler anemometry free from the measurement-volume effect. *Applied Optics*, 38(13):2737–2742, May 1999.
- C. M. Sipperley and W. D. Bachalo. Triple interval phase doppler interferometry: Improved dense sprays measurements and enhanced phase discrimination. In *17th International Symposium on Applications of Laser Techniques to Fluid Mechanics, Lisbon, Portugal*, Jul 2014.
- P. A. Strakey, D. G. Talley, S. V. Sankar, and W. D. Bachalo. Phase Doppler Interferometry with Probe-to-Droplet Size Ratios Less Than Unity. Part I: Trajectory Errors. *Applied Optics*, 39(22):3875–3886, Aug 2000.
- P. A. Strakey, D. G. Talley, S. V. Sankar, and W. D. Bachalo. Phase-doppler interferometry with probe-to-droplet size ratios less than unity. part ii. application of the technique. *Appl Opt*, 39:3887–3893, Aug 2000.

- J. M. Davis and P. J. Disimile. The effect of optical configuration selection on phase doppler anemometer fire suppressant nozzle characterizations. In *14th Halon Options Technical Working Conference*, May 2004.
- A. Taranenko. *Shattering Kraft Recovery Boiler Smelt by a Steam Jet*. PhD thesis, 2013.
- X. Jin. *Interaction between a Molten Smelt Droplet and Water at Different Temperatures*. PhD thesis, 2013.
- N. Dombrowski and P. C. Hooper. A study of the sprays formed by the impinging jets in laminar and turbulent flow. *Journal of Fluid Mechanics*, 18:392–400, 1964.
- R. Li and N. Ashgriz. Characteristics of liquid sheets formed by two impinging jets. *Physics of Fluids*, 18:7104, Aug 2006.